Entanglement of pygmy skin and core polarization modes in ^{206}Pb

N. Tsoneva and H. Lenske
Institut für Theoretische Physik, Universität Gießen

In this report we present our recent theoretical results on dipole response in the neutron-rich ^{206}Pb. The calculations are obtained in advanced microscopic theory of high predictive power, based on energy-density functional (EDF) and three-phonon quasiparticle-phonon model (QPM) [1, 2, 3]. In the focus of our studies are electric and magnetic dipole excitations with energies up to 25 MeV. Of special interest is the Pigmy Dipole Resonance (PDR) mode [3, 4] which incorporates the dynamics of the nuclear isospin at the nuclear surface. Thus, the PDR may provide useful information on fundamental properties of the nucleus such as neutron and proton root-mean-square radii, nuclear skin thickness and symmetry energy [5]. Despite of many experimental and theoretical evidences on the close relation between the PDR and the neutron skin, presently a direct method to extract experimentally the neutron skin thickness from the PDR does not exist [4]. This could be related to the fact that at excitation energies below the neutron separation energy the PDR coexists with a variety of modes, such as the tail of the GDR, magnetic dipole and multi-phonon excitations [2, 3]. So far the low-energy distribution of the GDR is elusive. The question that arises in this connection is how to differentiate the contributions of different origin to the low-energy photoabsorption spectra and in particular the PDR and GDR modes which are supposed to have the largest impact, in addition to other modes [3]. Theoretically, the problem could be solved within our three-phonon EDF+QPM approach which is one of the most elaborated multi-quasiparticle and multi-phonon approaches that has been proven successful in various scenarios [1, 2, 3, 6, 7].

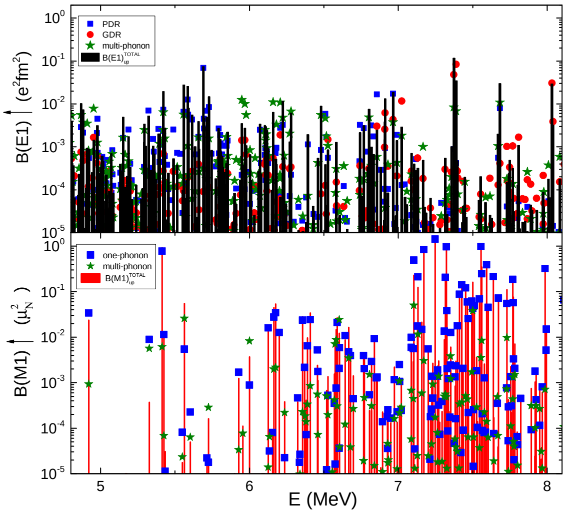

Figure 1: (Color online) B(E1) and B(M1) strength distributions of ^{206}Pb related to different counterparts of the transition matrix elements obtained from three-phonon EDF+QPM calculations.

Spectral distribution of the newly studied low-energy E1 and M1 strengths in ^{206}Pb (S_n = 8.087 MeV) are shown in Fig. 1. It is found that the fragmentation of the E1 strength is due to the interaction of the QRPA PDR states with those from the GDR tail and also with multi-phonon configurations with different spin and parities. The detailed EDF+QPM analysis of the E1 transition matrix elements strongly suggests that the PDR dominates the distribution of the dipole strength up to about 7 MeV, at which point the tail of the GDR starts making an important contribution. Overall, the PDR and the GDR account for about 77% and 12% of the $E1$ strength below the neutron separation energy in ^{206}Pb, respectively. Also significant is the impact from multi-phonon states to the total E1 strength—and to a lesser extent to the M1 strength. The theoretical cumulative electric and magnetic dipole strengths are compared to recent high-resolution ($\vec{\gamma}$,$\vec{\gamma}'$) experiment from the HI$\vec{\gamma}$S facility which provides spins, parities, branching ratios, and decay widths of excited states [5]. From the EDF+QPM calculations of both, E1 and M1 strengths up to 25 MeV in ^{206}Pb, we obtained also the total dipole polarizability α_D(^{206}Pb)=18.3 (fm^3/e^2) which is in good agreement with the HI$\vec{\gamma}$S data and earlier photonuclear experiments above the neutron threshold [5]. The comparison of the α_D value with the one obtained in ^{208}Pb [8] shows a decrease of $\approx$3% in ^{206}Pb. This is found correlated with the decrease of the neutron skin thickness of ^{206}Pb which value is $\approx$4% less than that of ^{208}Pb.

References

[1] N. Tsoneva *et al.*, **B586**, 213 (2004).

[2] N. Tsoneva, H. Lenske, Phys. Rev. C **77**, 024321 (2008).

[3] N. Tsoneva, H. Lenske, Physics of Atomic Nuclei, Vol. 76, pp. 885-903 (2016) and refs. therein.

[4] D. Savran *et al.*, Prog. Part. Nucl. Phys. **70**, 210 (2013).

[5] A. Tonchev *et al.*, Phys. Lett. B, submitted.

[6] N. Tsoneva, H. Lenske, Phys. Lett. B **695**, 174 (2011).

[7] N. Tsoneva *et al.*, Phys. Rev. C **91**, 044328 (2015).

[8] A. Tamii *et al.*, Phys. Rev. Lett. **107**, 062502 (2011).

DOI:10.15120/GR-2017-1

Gogny-HFB self-consistent blocking for odd-A and odd-odd nuclei[*]

A. Arzhanov[1,2], *G. Martínez Pinedo*[1,2], *L. M. Robledo*[3], *and T. R. Rodríguez*[3]
[1]Institut für Kernphysik, TU Darmstadt, D-64289 Darmstadt, Germany; [2]GSI Helmholtzzentrum für Schwerionenforschung, D-64291 Darmstadt, Germany; [3]Departamento de Física Teórica, UAM, E-28049 Madrid, Spain

Self-consistent blocking within Gogny-HFB

A self-consistent description of odd-A and odd-odd nuclei breaks the time-reversal symmetry. This makes their study more involved than the one of even-even nuclei in different aspects. In the case of Gogny energy density functional (EDF), the Hartree-Fock and pairing fields possess both T-even and T-odd components. For even-even nuclei the T-odd terms intricately vanish in the nuclear ground state calculations of $J^\pi = 0^+$ configurations, and therefore can be disregarded in numerical computations. However, for odd nuclei the T-odd fields have to be treated explicitly in the calculations. This fact lifts the two-fold Kramer's degeneracy of the HFB quasi-particles (q.p.) states, thereby at least doubling the computational effort already in this aspect. Moreover, a fully self-consistent variational calculation for odd nuclei usually requires to block multiple low-lying q.p. states separately to later identify the configuration leading to the lowest ground state energy solution, thereby making the calculation scheme even more sophisticated and time-consuming. Because of the heavy computational burden, most of the recent calculations either ignored the T-odd fields completely, or involved approximative blocking techniques while keeping the benefits of time-reversal symmetry.

Global survey

We have performed a large-scale self-consistent calculation including all T-odd components of Gogny EDF to calculate both odd-A and doubly odd nuclei up to the neutron drip lines from $Z = 8$ up to $Z = 134$. We have also employed the widely used perturbative quasiparticle addition (PQPA) approximative method, and compared the results from both methods with the experimental values.

Both PQPA and T-odd global calculations exhibit a common trend of decreasing spread of the neutron pairing gaps for heavier elements. In the case of PQPA, the gaps tend to decrease in their strength for heavier isotopic chains, which is not visible in the T-odd calculations. The systematic decrease of the gap strength with the mass number is also present for the experimental gaps (gray regions on the Fig.), which follow a general trend $\Delta_n^{(3)} \approx 12/\sqrt{A}$ MeV based on the global fit. Another feature on the global scale is the occurrence of many narrow dips in the PQPA results – particularly noticeable in the region $N \approx 50-120$. The T-odd gaps appear to be more smeared out, with only a couple of major well-established dips occurring in vicinity from the magic numbers $N = 28, 50, 82, 126$. Besides the fact that the PQPA approximation overall yield larger gaps than T-odd calculations, there is an apparent tendency of odd-Z gaps having weaker strength than in the even-Z chains. This feature is qualitatively visible in the Figure, where the odd-Z chains (blue) are shifted downwards with respect to the even-Z chains (red), whereas the PQPA calculatations clearly do not exhibit this feature. This is quantitatively verified: the calculated number of 1985 even-Z and the same number of odd-Z pairing gaps have an identical average of 0.95 MeV, whereas the T-odd calculations for the same nuclei have 0.73 MeV and 0.62 MeV for even-Z and odd-Z cases, respectively. This dependence on proton number parity is also established experimentally, where the total number of 556 even-Z gaps are found to have 1.06 MeV, while the 508 established odd-Z gaps yield 0.76 MeV on average. Interestingly, the standard deviation in all the cases of calculated gaps is found to be $\sim$0.28 MeV.

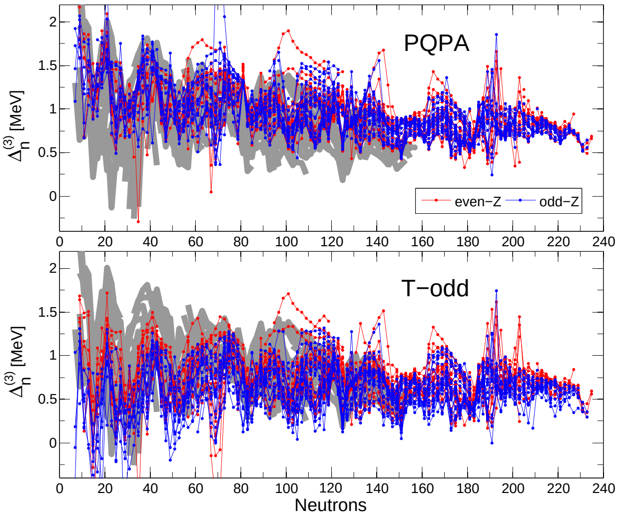

Figure 1: Pairing gaps from PQPA (upper panel) and T-odd (lower panel) even-Z (red) and odd-Z (blue) calculations. Gray region represents experimental pairing gaps.

Overall, the pairing strength of D1S functional is adequate to describe important qualitative features of the experimentally known gaps, but their mass dependence is not very well reproduced in T-odd calculations. Ultimately, in order to improve the theoretical results, the T-odd interaction should be re-examined, while also exploring the impact of beyond-mean-field correlations.

---

[*] Work supported by Helmholtz Association through Nuclear Astrophysics Virtual Institute (VH-VI-417 /HGF/ NAVI GSI).

DOI:10.15120/GR-2017-1

The Wigner function of the deuteron

T. Neff[1] *and H. Feldmeier*[1,2]
[1]GSI, Darmstadt, Germany; [2]FIAS, Frankfurt, Germany

Short-range correlations in nuclei are induced by the strong repulsion and the strong tensor force found in realistic nucleon-nucleon interactions. They are usually investigated in coordinate space where they are reflected in a suppression of the two-body density at short distances or in momentum space where they manifest themselves in high-momentum components of one- and two-body densities [1]. This short-range physics is usually contrasted with the low momentum part that contains mainly long-range correlations which are describable by superpositions of a smaller number of uncorrelated Slater determinants.

To provide a better intuitive picture for how long- and short-range or low- and high-momentum physics are connected we decided to investigate the Wigner function of the deuteron. The Wigner function or Wigner representation is the quantum mechanical analogue of the classical phase space distribution [2] and contains the full information about the system as given by its wave function or the density matrix.

$$W(\vec{r},\vec{p}) = \frac{1}{(2\pi)^3}\int d^3s\,\left\langle \vec{r}+\tfrac{1}{2}\vec{s}\right|\widehat{\rho}\left|\vec{r}-\tfrac{1}{2}\vec{s}\right\rangle e^{-i\vec{p}\cdot\vec{s}} \quad (1)$$

$$= \frac{1}{(2\pi)^3}\int d^3\varkappa\,\left\langle \vec{p}+\tfrac{1}{2}\vec{\varkappa}\right|\widehat{\rho}\left|\vec{p}-\tfrac{1}{2}\vec{\varkappa}\right\rangle e^{i\vec{\varkappa}\cdot\vec{r}}$$

The Wigner function furthermore makes a comparison with the classical picture possible and highlights the quantum-mechanical nature of short-range correlations.

The Wigner functions $W(r,p)$ obtained with realistic AV8' and N3LO interactions show a characteristic behavior. One can distinguish between a dominant low-momentum region that is unaffected by short-range correlations and a high-momentum region that shows a shoulder at distances up to 1.5 fm and that extends to high relative momenta. Another characteristic feature is an oscillating behavior of the Wigner function extending to large arguments $rp \approx \mathrm{const.}$. The contribution of short-range correlations is highlighted when the Wigner functions for the bare AV8' and N3LO interactions (as shown in Fig. 1 are compared to those obtained with softened interactions in the SRG approach. The SRG transformation decouples low- and high-momentum modes and essentially eliminates short-range correlations. This is reflected in the Wigner functions that are very similar to those obtained with the bare interactions in the low-momentum region, but that become more and more suppressed in the high-momentum region with increasing flow parameter. If the Wigner function is interpreted as a quasi-probability distribution one can define partial momentum distributions that are obtained by integrating over pairs at small and large distances respectively.

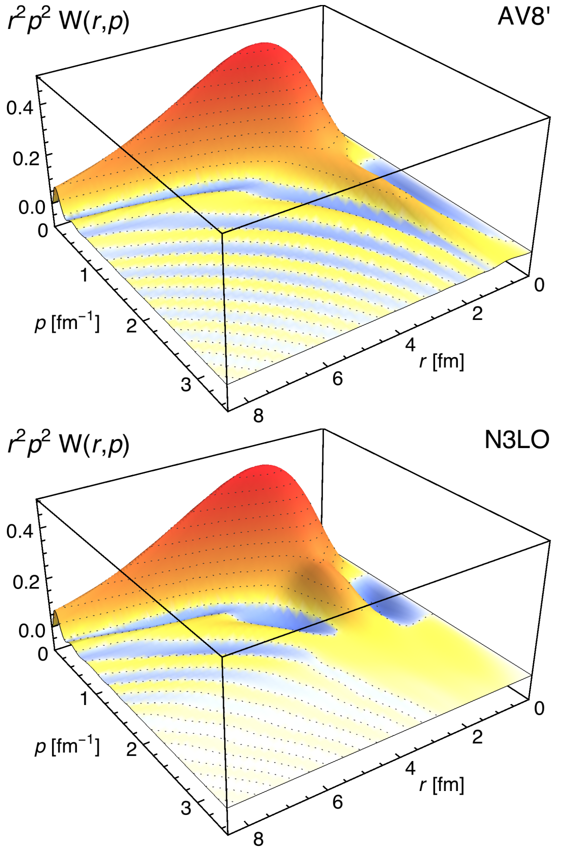

Figure 1: Wigner functions of the deuteron scaled with phase space volume element $r^2p^2W(r,p)$ for the AV8' interaction (top) and the chiral N3LO interaction (bottom).

In case of the AV8' interaction there is a clear separation between a small- and large distance scale. Pairs at small distances generate the high-momentum components. This separation is not so clear for the N3LO interaction. This interaction contains regulators that affect the wave function even at large distances and generate high-momentum components.

References

[1] T. Neff, H. Feldmeier, W. Horiuchi, Phys. Rev. C **92**, 024003 (2015).

[2] E. Wigner, Phys. Rev. C **40**, 749 (1932).

[3] T. Neff, H. Feldmeier, arXiv:1610.04066

The ν process in core-collapse supernova nucleosynthesis [*]

A. Sieverding[†][1], *G. Martínez-Pinedo*[1,2], *and K. Langanke*[2,1]

[1]Institut für Kernphysik (Theoriezentrum), Technische Universität Darmstadt, Schlossgartenstraße 2, 64289 Darmstadt, Germany; [2]Gesellschaft für Schwerionenforschung Darmstadt, Planckstr. 1, D-64259 Darmstadt, Germany

Supernova explosions mark the end of the lives of stars that are born more massive than 8-10 $\mathrm{M}_\odot$ and are accompanied by the emission of a large number of neutrinos of all flavors from the collapsing stellar core which are not only important for the explosion itself but also interact with the bulk of the stellar material which is finally ejected. Neutrino-nucleus interactions can lead to inverse beta-decay (charged-current) and nuclear excitations above particle separation threshold (charged- and neutral-current). Emitted light particles then provide additional fuel for further thermonuclear reactions. These direct and indirect effects of neutrinos are referred to as the ν process. Compared to previous studies of this process [1] that have assumed average neutrino energies of $\langle E_{\nu_e} \rangle = 13$ MeV, $\langle E_{\bar{\nu}_e} \rangle = 15$ MeV and $\langle E_{\nu,\bar{\nu}_{\mu,\tau}} \rangle = 19$ MeV recent progress in supernova simulations has corrected the expected neutrino energies significantly downward to values around $\langle E_{\nu_e} \rangle = 9$ MeV, $\langle E_{\bar{\nu}_e} \rangle = \langle E_{\nu,\bar{\nu}_{\mu,\tau}} \rangle = 13$ MeV. This results in a general reduction of the effect of the ν process but also in a larger sensitivity to charged-current reactions that proceed through low-lying transitions. This has motivated the effort to derive charged-current neutrino nucleus cross sections from experimentally measured data [2]. We have performed a set of nucleosynthesis calculations for a range of supernova progenitor models with initial masses between 13-30 $\mathrm{M}_\odot$ presented in [4] using parametric explosion models based on the hydrodynamics code KEPLER which is a significant improvement compared to the results presented in [3]. The model is tuned to achieve an explosion energy of 1.2×10^{51} erg for all progenitor models and we assume that 3×10^{53} erg are emitted as neutrinos equally distributed over all 6 flavors.

Nucleus	no ν	Low energies	High energies
^{7}Li	0.002	0.07	0.45
^{11}B	0.008	0.36	1.54
^{19}F	0.12	0.19	0.33
^{138}La	0.12	0.55	1.15
^{180}Ta	0.19	0.49	0.88

Table 1: Production factors relative to solar abundances normalized to ^{16}O production without neutrinos, with our choice of neutrino energies (“Low energies”), and with the choice of ref. [1] (“High energies”). For ^{180}Ta we assume that 35% survive in the long-lived isomeric state

Table 1 shows the production factors we have obtained comparing calculations without neutrinos to the probably more realistic low energy neutrinos and also the “canonical” neutrino energies averaged over the progenitor mass with progenitor masses distributed according to the empirical Salpeter initial mass function $\mathrm{d}n_*/\mathrm{d}m_* \propto m_*^{-1.35}$. With the low neutrino energies the ν process cannot account for the production of the light elements ^{7}Li and ^{11}B and ^{19}F to full solar abundance. However, for ^{7}Li and ^{11}B irradiation by galactic cosmic rays can provide an additional contribution. ^{138}La and ^{180}Ta remain as the most sensitive to neutrino interactions and could be produced predominantly by the ν process. We have also explored the production of the radioactive isotopes ^{26}Al, ^{44}Ti and ^{60}Fe that are important for γ-ray astronomy that are summarized in table 2. Especially for low energies we find only minor effects for ^{26}Al and almost no effect for ^{44}Ti and ^{60}Fe. However, we find quite a significant enhancement of the production of ^{22}Na that has been found in pre-solar grains of supernova origin.

Nucleus	no ν	Low energies[1]	High energies[2]
^{22}Na	2.41×10^{-6}	3.02×10^{-6}	3.74×10^{-6}
^{26}Al	4.29×10^{-5}	4.64×10^{-5}	5.27×10^{-5}
^{44}Ti	1.48×10^{-5}	1.49×10^{-5}	1.56×10^{-5}
^{60}Fe	7.58×10^{-5}	7.53×10^{-5}	7.56×10^{-5}
^{92}Nb	4.53×10^{-11}	9.69×10^{-11}	16.73×10^{-11}
^{98}Tc	2.84×10^{-11}	3.38×10^{-11}	4.10×10^{-11}

Table 2: Yields of of radioactive isotopes in $\mathrm{M}_\odot$ averaged over progenitor masses for different choices of neutrino energies

References

[1] A. Heger, E. Kolbe, W. Haxton, K. Langanke, G. Martínez-Pinedo, S. E. Woosley, “Neutrino nucleosynthesis”, Phys. Lett. B 606, 258

[2] A. Sieverding, , G. Martínez-Pinedo, T. Marketin, K. Langanke , “Charged-current neutrino-nucleus cross-sections for the ν process” , GSI Scientific Report 2015 (2016), 242

[3] A. Sieverding , G. Martínez-Pinedo, K. Langanke “Neutrino Nucleosynthesis of radioactive nuclei in supernovae” , GSI Scientific Report 2014 (2015), 341

[4] A. Heger, S. E. Woosley, “Nucleosynthesis and remnants in massive stars of solar metallicity” Physics Reports 442 (2007), 269

---

[*] Work supported by NAVI and by the DFG through SFB 1245

[†] a.sieverding@gsi.de

r-process abundances from BCPM fission properties[*]

S. A. Giuliani[†1], *G. Martínez-Pinedo*[1,2], *L. M. Robledo*[3], *and M.-R. Wu*[4]

[1]Institut für Kernphysik (Theoriezentrum), Technische Universität Darmstadt, Schlossgartenstraße 2, 64289 Darmstadt, Germany; [2]GSI Helmholtzzentrum für Schwerioneneforschung, Planckstraße 1, 64291 Darmstadt, Germany; [3]Departamento de Física Teórica, Universidad Autónoma de Madrid, E-28049 Madrid, Spain.; [4]Niels Bohr International Academy, Niels Bohr Institute, Blegdamsvej 17, 2100 Copenhagen, Denmark

The r-process is invoked in order to explain the existence of nuclei heavier than iron that are observed in the Universe. Even though its astrophysical site is not (yet) known, recent simulations suggest the merger of two neutron star (NSM) as a likely candidate. In such astrophysical site seed nuclei can capture a large number of free neutrons reaching the fissioning region by successive neutron-captures and beta-decays. In this case fission plays a crucial role by terminating the r-process path, shaping the second peak and providing a mechanism for robust abundances [1]. In this report, we present the results of r-process calculations for dynamical ejecta in NSM based on the fission properties computed using the Barcelona-Catania-Paris-Madrid (BCPM) energy density functional (EDF) [2, 3].

In a recent publication we studied the fission properties of r-process nuclei predicted by the BCPM EDF [4]. We consistently computed fission barriers, collective inertias and neutron separation energies and used them as a nuclear input for the calculation of stellar reactions rates of neutron-induced reactions relevant for r-process in the region $84 \leq Z \leq 120$ and $118 \leq N \leq 250$. The rates were obtained within the statistical theory using the Back-shifted Fermi gas model for level densities and the Kopecky-Uhl generalized Lorentzian gamma-ray strength functions implemented in the TALYS code. Fig. 1 shows the final r-process abundances obtained from the BCPM neutron-induced stellar rates for a single standard trajectory simulating the dynamic ejecta in neutron star mergers. For comparison, the plot also shows the abundances obtained from the neutron-induced stellar rates computed by Panov *et al.* [5] based on the FRDM nuclear masses and Thomas-Fermi fission barriers.

Our calculations predict larger barriers and shell gaps for nuclei around the magic number $N = 184$. This results in a larger accumulation of material in the region $A \sim 280$. Lately this material decays by fission enhancing the abundances above the second peak ($A \sim 150$). Conversely, the larger shell gap predicted by the FRDM mass model around $N = 172$ induces an accumulation of material at $A \sim 257$ that enhances the abundances below the second peak $A \sim 110$. These results prove the extreme sensitivity of the r-process abundances to local variations in the binding energies and to the fission properties of the r-process nuclei. On the other hand, comparing the ratio of the ^{232}Th and ^{238}U cosmochronometers and the radioactive energy emitted at timescales relevant for macronova observations we did not find a significant difference between both models. This suggests that in both calculations the production of actinides during the build up of heavy nuclei is similar [6], which is due to the fact that we only changed the rates of nuclei with $Z \geq 84$.

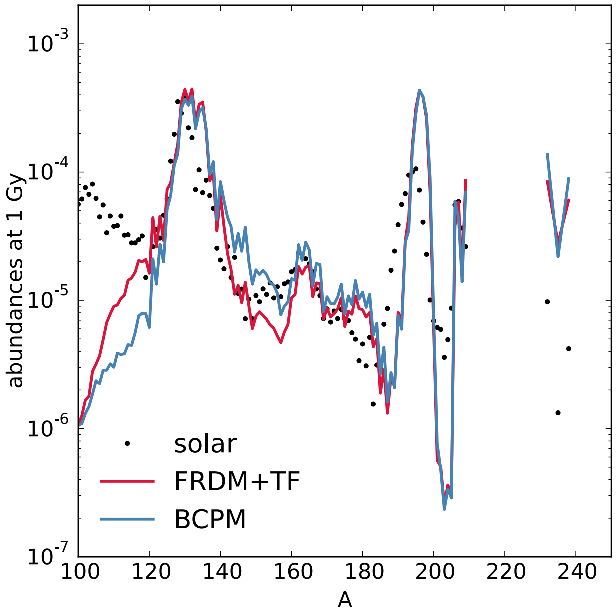

Figure 1: r-process abundances for two different sets of neutron-induced stellar rates: BCPM (blue line) and Panov et al. [5] (red line) at 1 Gy. Circles represent the solar r-process relative abundances.

References

[1] J. J. Mendoza-Temis et al., Phys. Rev. **C92**, 055805 (2015).

[2] M. Baldo et al., Phys. Rev. **C87**, 064305 (2013).

[3] S. A. Giuliani et al., Phys. Rev. **C88**, 054325 (2013).

[4] S. A. Giuliani, G. Martinez-Pinedo and L. M. Robledo, arXiv:1704.00554 [nucl-th].

[5] I. V. Panov et al., *Astron. Astrophys.* **513**, A61 (2010).

[6] J. Barnes et al., Astrophys. J. **829**, no. 2, 110 (2016)

---

[*] SAG, GMP and MRW acknowledge support from the the Helmholtz Association through the Nuclear Astrophysics Virtual Institute (VH-VI-417), and the BMBF-Verbundforschungsprojekt number 05P15RDFN1. MRW acknowledges support from the Villum Foundation (Project No. 13164) and the Danish National Research Foundation (DNRF91). The work of LMR was supported in part by the Spanish Ministerio de Economía y Competitividad (MINECO), under Contracts Nos. FIS2012-34479, FPA2015-65929, FIS2015-63770 and by the Consolider-Ingenio 2010 Program MULTIDARK.

[†] giuliani@theorie.ikp.physik.tu-darmstadt.de

Form-factor dependence of neutrino-nucleon interactions in supernova environment*

A. Lohs[1] *and G.Martinez-Pinedo*[1]
[1]GSI, Darmstadt, Germany

Highly energetic neutrinos in compact stellar objects are able to probe the weak form factor of (quasi)free nucleons to a sizeable extent. We present an implementation of this form factor dependence in the computation of the neutrino inverse mean free path in order to model more accurately the transport of neutrinos in dense baryonic matter.

Introduction

In semileptonic neutrino-nucleon reactions, such as (anti)neutrino absorption or scattering, the momentum transfer dependence of the weak nucleon form factors modifies the cross-section at 2nd order in neutrino energy over nucleon mass, $(E_\nu/m_N)^2$. For highly energetic supernova neutrinos in the range of several tens of MeV, these corrections need to be considered to accurately model many aspects of neutrino transport e.g. neutrino spectra formation or the neutrino driven wind (see e.g.[1]).

For the conditions which are present in astrophysical scenarios such as core-collapse supernovae or neutron star mergers, the dominating weak neutrino-nucleon interactions can be sufficiently described by a current-current Lagrangian with effective weak nucleon couplings. These nucleon couplings are sensitive to the momentum transfer, since highly energetic neutrinos are able to probe the nucleon's structure. The corresponding weak nucleon form factors can be directly related to the electromagnetic ones which are experimentally better accessible. For the important axial-vector coupling one finds

$$G_A\left(q^2\right) = G_A(0)\left(1-\frac{q^2}{m_A^2}\right)^{-2}, \text{with } m_A \simeq 1.206\,\mathrm{GeV}$$

where m_A is the so called axial mass. Similar relations are found for the vector coupling G_V and the tensor coupling F_2.

Recently we were able to explicitly include this behaviour in the semianalytic computation of the cross sections for these reactions, i.e. into the phase space integration over the reaction matrix element. Describing the strong interaction among the nucleons in the framework of *relativistic mean field*, one can show that for all the different couplings in the effective nucleon current the form factor dependence is well approximated by the relation

$$G_X G_Y\left(q^2\right) = G_X G_Y(0)\left(1+\frac{4q^2}{m_{XY}^2}\right)$$

The pure vector component G_V^2 for example is described by $1/m_{VV}^2 = 1/M_V^2 - F_2(0)/8m_N$, where $M_V \simeq 0.84\,\mathrm{GeV}$ is the so called vectorial mass.

Results

Using the above relation one can compute the inverse mean free path $1/\lambda(E_\nu)$ from a simple 2D-numerical integral, without the need for further simplifications regarding the kinematics or the degree of relativity of any of the participating particles. For representative conditions at the neutrinosphere, the quenching of the energy dependent inverse mean free path is shown in Fig.1 for (anti)neutrino absorption on neutrons (protons) by the solid (dashed) curve.

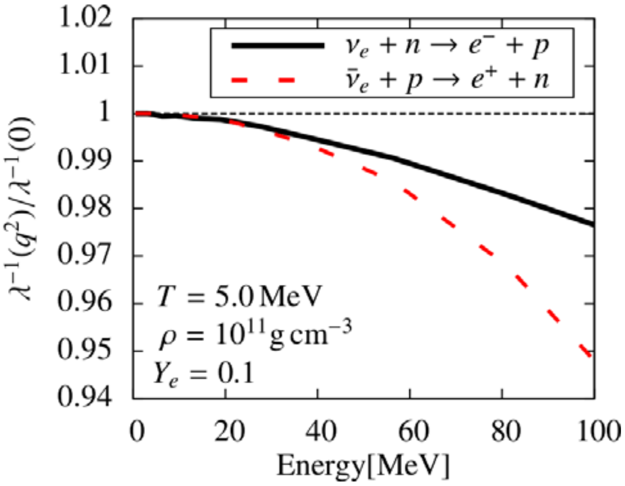

Figure 1: Quenching of neutrino inverse mean free path due to weak nucleon form factor.

The quenching is larger for $\bar{\nu}_e$ compared to ν_e. In general it is smaller than 1% for neutrino energies below $40-50\,\mathrm{MeV}$, and it just reaches 5% for antineutrinos with $E_{\bar{\nu}_e} \sim 100\,\mathrm{MeV}$. While we expect a rather small impact on the emerging neutrino spectra, we still recommend the inclusion of this effect when considering nucleon recoil effects, since it adds no further numerical complexity.

References

[1] C.J. Horowitz,"Weak magnetism for antineutrinos in supernovae", Phys.Rev. D65 (2002) 043001

---

* The work of A.L. is partly supported by GSI, University of Basel, and by the Helmholtz Association through the Nuclear Astrophysics Virtual Institute (VH-VI-417).

High-mass twin neutron stars with hybrid equations of state and the existence of a critical end point in the QCD phase diagram*

S. Typel† [1,2], *D. Alvarez-Castillo*[3], *and D. Blaschke*[3,4,5]

[1]IKP, TU Darmstadt, Darmstadt, Germany ; [2]GSI, Darmstadt, Germany; [3]BLTP, JINR, Dubna, Russia; [4]National Research Nuclear University (MEPhI), Moscow, Russia; [5]ITP, University of Wrocław, Wrocław, Poland

The equation of state (EoS) of strongly interacting matter at almost vanishing temperature and baryon densities above the nuclear saturation density determines fundamental properties of neutron stars and in particular their mass-radius relation. The observation of compact stars with precisely determined masses around two solar masses [1, 2, 3] puts already severe constraints on models for high-density matter [5] requiring a rather stiff EoS. In contrast, present-day measurements of neutron star radii give ambiguous results and still suffer from large uncertainties. Future x-ray satellite mission like NICER [4] are expected to provide more precise constraints on compact star radii.

A sufficiently strong first-order phase transition from hadronic to deconfined quark matter could affect the mass-radius relation with the possible existence of a third family of compact stars. The observation of "mass twins", i.e. compact stars with the same mass but a measurable radius difference of about $1 - 2$ km, and a gap in the mass-radius relation would support the existence of at least one critical end point (CEP) in the QCD phase diagram [6] because lattice QCD calculations established that the transition from hadronic to quark matter is a crossover on the temperature axis at zero baryochemical potential, see, e.g., [7, 8].

The consequences of a first-order phase transition on the structure of compact stars can be explored by providing suitable EoSs of the hadronic and quark matter phases for the construction of the phase transition with the conditions of β equilibrium and charge neutrality. A generalized relativistic density functional with well calibrated density dependent couplings [9], which fulfills most current constraints from nuclei and nuclear matter, is used for the microscopic description of the hadronic phase. Excluded-volume effects are considered at suprasaturation densities in the thermodynamically consistent approach of Ref. [10] that can model a stiffening or softening of the EoS employing effective, density-dependent degeneracy factors. This homogeneous neutron star matter EoS is supplemented by an appropriate crust EoS at densities below nuclear saturation. Quark matter is described in a QCD motivated extended Nambu–Jona-Lasinio model with higher-order interactions [11] that allows a stiffening of the EoS by a variation of the eight-quark coupling parameter. The two-phase/hybrid EoS is prepared from the two models using the standard Maxwell construction assuming a coexistence of both phases with macroscopic size neglecting surface effects. The Tolman-Oppenheimer-Volkoff equations are solved to generate sequences of compact stars and the resulting mass-radius relations for various parameter sets.

A Bayesian analysis of the parameter dependence for the hybrid EoSs has been performed with given observational constraints for the mass and radius of compact stars [12]. It was shown that the observation of high-mass twin stars would have the power to discriminate between hybrid EoS models with strong first-order phase transitions and alternative EoS models. In addition, it was observed that there is a correlation between the maximum radius of the horizontal branch in the mass-radius diagram and the pressure at the onset of the hadron-to-quark matter transition. This is likely a quantity of utmost relevance for upcoming experiments with heavy-ion collisions (HICs) at FAIR and NICA. It is in striking agreement with the "universal" hadronization pressure extracted from the analysis of chemical freeze-out in HICs [13].

In the future, the robustness of the high-mass twin-star phenomenon with respect to the precise form of the hadron-to-quark phase transition has to be investigated, in particular by considering a mixed phase where pasta-like structures appear [14] similar as at the crust-core boundary in neutron stars.

References

[1] P. Demorest *et al.*, Nature **467** (2010) 1081

[2] J. Antoniadis *et al.*, Science **340** (2013) 6131

[3] E. Fonseca *et al.*, Astrophys. J. **832** (2016) 167

[4] K. C. Gendreau *et al.*, Proc. SPIE **9905** (2016) 99051H

[5] M. Oertel, M. Hempel, T. Klähn and S. Typel, Rev. Mod. Phys. **89** (2017) 015007

[6] D. Alvarez-Castillo, S. Benic, D. Blaschke, S. Han and S. Typel, Eur. Phys. J. A **52** (2016) 232

[7] S. Borsanyi *et al.*, Phys. Lett. B **730** (2014) 99

[8] A. Bazavov *et al.* [HotQCD Collaboration], Phys. Rev. D **90** (2014) 094503

[9] S. Typel *et al.*, Phys. Rev. C **81** (2010) 015803

[10] S. Typel, Eur. Phys. J. A **52** (2016) 16

[11] S. Benic, D. Blaschke, D. E. Alvarez-Castillo, T. Fischer and S. Typel, Astron. Astrophys. **577** (2015) A40

[12] D. Alvarez-Castillo, A. Ayriyan, S. Benic, D. Blaschke, H. Grigorian and S. Typel, Eur. Phys. J. A **52** (2016) 69

[13] M. Petran and J. Rafelski, Phys. Rev. C **88** (2013) 021901

[14] D. E. Alvarez-Castillo and D. Blaschke, Phys. Part. Nucl. **46** (2015) 846

---

* Work supported by COST action MP 1304 "NewCompStar", Polish NCN under grant No. UMO-2014/13/B/ST9/02621, Heisenberg-Landau programme, Bogoliubov-Infeld programme, LOEWE, HIC for FAIR, HGF, and NAVI (VH-VI-417).

† s.typel@gsi.de

DOI:10.15120/GR-2017-1

Matter in neutron star mergers vs. matter in heavy ion collisions*

A. Mukherjee†[1], *J Steinheimer*[1], *S. Schramm*[1,2], *and H. Stöcker*[1,2,3]
[1]Frankfurt Institute for Advanced Studies; [2]Institut für Theoretische Physik, Goethe Universität, Frankfurt am Main;
[3]GSI Helmholtzzentrum für Schwerionenforschung GmbH

Gravitational waves (GWs) have been recently observed from a pair of merging black holes (BHs) by the LIGO detectors [1] and GWs emitted from merging neutron star (NS) binaries are on the verge of their first detection. The equation of state (EOS) of elementary matter might be deduced by a frequency analysis of the GW [2, 3], which is interesting, as the EOS of quantum chromo dynamics (QCD) is mainly investigated by high energy heavy ion collisions. In heavy ion experiments at particle accelerators, heavy nuclei collide to create a small system which is expected to have a Temperature of $T \geq 80$ MeV and densities several times the nuclear ground state density. It is therefore very intriguing to study QCD matter at similar temperatures and densities in two rather different 'experimental' setups, in neutron star mergers and heavy ion collisions.

Densities in NS mergers and nuclear collisions

In order to determine the temperature of the system at given densities, one requires knowledge on the effective degrees of freedom of the system, encoded in the equation of state. Depending on the EOS used, the Temperatures reached in these relativistic collisions and neutron star mergers may vary significantly. It is consequently most important to employ an EOS that entails a realistic set of degrees of freedom as well as interactions.

The model we employed is the so called Quark-Hadron Chiral Parity Doublet Model (QχP) [4, 5]. This approach describes the thermodynamics of the transition from a hadronic chiral model to a deconfined quark phase.

A straight forward way of consistently connecting the features of the EOS with the maximally achievable compression of a relativistic collision is by employing the so called Rankine-Hugoniot-Taub-Adiabat [6]. If the EoS, i.e. the connection between pressure, energy density and baryon density is know (as p(ϵ,ρ)), then one can calculate the maximum compression in a collision by solving the following Taub-equation:

$$(\rho_0\, X_0)^2 - (\rho\, X)^2 - (p_0 - p)(X_0 + X) = 0 \qquad (1)$$

with $X = (\epsilon + p)/\rho^2$, the generalized volume. For simplicity we assume $p_0 = 0$. One can furthermore connect the center of mass gamma factor $\gamma_{\rm c.m.}$ of the colliding slabs to the densities created using $\gamma^2_{\rm c.m.} = \left(\frac{\epsilon\ \rho_0}{\rho\ \epsilon_0}\right)^2$. The resulting beam energy dependence of the net-baryon density and temperatures reached is shown in figure 1 (left) for two different scenarios:

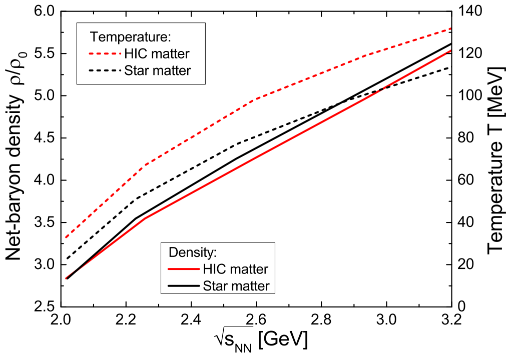

Figure 1: Largest net-baryon density (solid lines) and Temperatures (dashed lines) achieved in collisions of heavy ions and compact stars at a given center of mass beam energy $\sqrt{s_{\rm NN}} = 2 \cdot \gamma_{\rm c.m.} \cdot m_N$. Due to the different properties of the EoS as function of iso-spin the temperatures in heavy ion collisions are larger and densities slightly smaller, at the same relative velocities.

1. The EOS for heavy ion collisions, i.e. with conserved strangeness and no beta-equilibrium
2. The EOS for compact stars, i.e. in beta-equilibrium

Figure 1 presents, for different center of mass energies, the compressions achieved, using the Rankine-Hugoniot-Taub-Adiabat with the QχP EOS. This figure highlights the difference in the compression in collisions of projectiles with iso-spin symmetric matter (heavy ion collisions) and asymmetric matter (NS mergers).

References

[1] B. P. Abbott *et al.* [LIGO Scientific and Virgo Collaborations], Phys. Rev. Lett. **116**, no. 6, 061102 (2016).

[2] K. Takami, L. Rezzolla and L. Baiotti, Phys. Rev. Lett. **113**, no. 9, 091104 (2014).

[3] L. Rezzolla and K. Takami, Phys. Rev. D **93**, no. 12, 124051 (2016).

[4] A. Mukherjee, J. Steinheimer and S. Schramm, arXiv:1611.10144 [nucl-th].

[5] J. Steinheimer, S. Schramm and H. Stocker, Phys. Rev. C **84**, 045208 (2011)

[6] A. H. Taub, Phys. Rev. **74**, 328 (1948).

---

[*] Work supported by GSI, BMBF, HIC4FAIR and HGShire.

[†] mukherjee@fias.uni-frankfurt.de

DOI:10.15120/GR-2017-1

Equation of state dependence of directed flow in a microscopic transport model[*]

Yasushi Nara[†][1,2], *Harri Niemi*[3], *Jan Steinheimer*[2], *and Horst Stöcker*[2,3,4]

[1]Akita International University, Yuwa, Japan; [2]Frankfurt Institute for Advanced Studies; [3]Institut für Theoretishe Physik, Johann Wolfgang Goethe Universität; [4]GSI Helmholtzzentrum für Schwerionenforschung GmbH

The collective transverse flow measured in the heavy ion collisions is considered to be sensitive to the equation of state (EoS) of QCD matter. The softest region in the EoS with a (first-order) phase transition is expected to have significant influence on the directed flow $v_1 = \langle \cos\phi \rangle$ of nucleons [1, 2].

In this work [3], we shall examine effects of the EoS on the directed flow within the microscopic transport approach JAM by modifying the scattering style in the two-body collision term [4, 5]. In JAM [6], particle production is modeled by the excitation and decay of resonances and strings. In the standard cascade approach the two body collision term is implemented so that it does not generate additional pressure. Namely, the azimuthal angle in the two-body collision is randomly chosen. It is well known that the pressure can be controlled by changing the scattering style. Here we employ a method similar to that proposed in Ref. [4] in which the momentum change in each two-body collision between particle i and j at the space-time coordinates of q_i and q_j is related to the pressure $\Delta P = P - P_f$, where P_f is the free streaming part of the local pressure. The formula is given by $\Delta P = -\frac{\rho}{3(\delta\tau_i+\delta\tau_j)}(p'_i - p_i)^\mu (q_i - q_j)_\mu$, where ρ is the Lorentz invariant local particle density, $\delta\tau_i$ is the proper time interval between successive collisions, and $p'_i - p_i$ is the energy-momentum change of the particle i. P_f can be computed from the energy-momentum tensor $T^{\mu\nu}$: In this way, we control the pressure such that P coincides with any given EoS at an energy density $e = u_\mu T^{\mu\nu} u_\nu$.

In Fig. 1 we present the beam energy dependence of the slope of the directed flow dv_1/dy of protons in mid-central A+A collisions. The standard JAM cascade calculation predicts a minimum at around AGS energy. In the case of the EoS with the first order phase transition (JAM-1.Opt), we also see the minimum in the excitation function of the proton directed flow at almost the same beam energy as the cascade model. In addition, the slope is now negative as predicted by hydrodynamical approaches.

We therefore have shown that our approach provides an efficient method to control the EoS in a microscopic transport model, and our result yields qualitatively similar result as the pure hydrodynamical predictions. As predicted by hydrodynamical approach, the minimum of the directed flow, from a strong first order phase transition, is located at much lower beam energy than the STAR data.

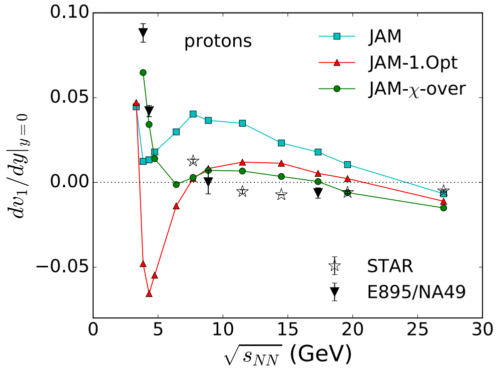

Figure 1: Beam energy dependence of the slope of the directed flow of protons in mid-central Au+Au collisions (10-40%) from JAM cascade mode (squares), JAM with first-order EoS (triangles) and with crossover EoS (circles) in comparison with the STAR/NA49/E895 data [7, 8, 9, 10, 11]. Local energy densities are computed by taking into account the contributions of constituent quarks.

References

[1] D. H. Rischke, Y. Pursun, J. A. Maruhn, H. Stoecker and W. Greiner, Heavy Ion Phys. **1**, 309 (1995)

[2] H. Stoecker, Nucl. Phys. A **750**, 121 (2005)

[3] Y. Nara, H. Niemi, J. Steinheimer and H. Stöcker, doi:10.1016/j.physletb.2017.02.020

[4] H. Sorge, Phys. Rev. Lett. **82**, 2048 (1999)

[5] Y. Nara, H. Niemi, A. Ohnishi and H. Stöcker, Phys. Rev. C **94**, no. 3, 034906 (2016)

[6] Y. Nara, N. Otuka, A. Ohnishi, K. Niita and S. Chiba, Phys. Rev. C **61**, 024901 (2000).

[7] L. Adamczyk *et al.* [STAR Collaboration], Phys. Rev. Lett. **112**, no. 16, 162301 (2014).

[8] P. Shanmuganathan [STAR Collaboration], Nucl. Phys. A **956**, 260 (2016)

[9] H. Liu *et al.* [E895 Collaboration], Phys. Rev. Lett. **84**, 5488 (2000);

[10] H. Appelshauser *et al.* [NA49 Collaboration], Phys. Rev. Lett. **80**, 4136 (1998);

[11] C. Alt *et al.* [NA49 Collaboration], Phys. Rev. C **68**, 034903 (2003).

---

[*] This work was supported in part by the Grants-in-Aid for Scientific Research from JSPS (Nos. 15K05079 and 15K05098), H. N. has received funding from the European Union's Horizon 2020 research and innovation programme under the Marie Sklodowska-Curie grant agreement no. 655285 and from the Helmholtz International Center for FAIR within the framework of the LOEWE program launched by the State of Hesse.

[†] nara@aiu.ac.jp

DOI:10.15120/GR-2017-1

Traces of non-equilibrium dynamics in relativistic heavy-ion collisions*

P.Moreau[1,2,3], *Y. Xu*[4], *T. Song*[1,2,5], *M. Nahrgang*[4,6], *S. A. Bass*[4], *and E. Bratkovskaya*[2,3]
[1]Frankfurt Institute for Advanced Studies, Johann Wolfgang Goethe Universität, Frankfurt am Main, Germany; [2]Institute for Theoretical Physics, Johann Wolfgang Goethe Universität, Frankfurt am Main, Germany; [3]GSI Helmholtzzentrum für Schwerionenforschung GmbH, Planckstrasse 1, 64291 Darmstadt, Germany; [4]Department of Physics, Duke University, Durham, NC 27708, USA; [5]Institut für Theoretische Physik, Universität Gießen, Heinrich-Buff-Ring 16, 35392 Gießen, Germany; [6]SUBATECH UMR 6457 (IMT Atlantique, Université de Nantes, IN2P3/CNRS), 4 rue Alfred Kastler, 44307 Nantes, France

In this contribution, we summarize our work from [1] where we performed a comparison of two prominent models for the evolution of bulk QCD matter. The first one is a non-equilibrium transport approach, the Parton-Hadron-String-Dynamics (PHSD) [2, 3, 4], and the second one a 2D+1 viscous hydrodynamical model, VISHNew [5, 6] which is based on the assumption of local equilibrium and conservation laws. Both approaches give an excellent agreement with numerous experimental data, despite the very different assumptions inherent in these models. In PHSD, quasi-particles are treated in off-shell transport with thermal masses and widths which reproduce the lattice QCD equation of state and are determined from parallel event runs in the simulations. Hydrodynamics assumes local equilibrium to be reached in the initial stages of heavy-ion collisions and transports energy-momentum and charge densities according to the lattice QCD equation of state and transport coefficients such as the shear and bulk viscosity.

We have tried to match the hydrodynamical evolution as closely as possible to quantities like viscosities as obtained within PHSD. In general we find that the ensemble averages over PHSD events follow closely the hydrodynamical evolution. The major differences between the macroscopic near-(local)-equilibrium and the microscopic off-equilibrium dynamics can be summarized as:

1. The hydrodynamical response to changing transport coefficients, especially the bulk viscosity, has a strong impact on the time evolution of the momentum anisotropy. In PHSD these transport coefficients can be determined but remain intrinsically linked to the interaction cross sections. Although there are indications for a substantial bulk viscosity in PHSD, it does not show the same sensitivity to the momentum space anisotropy as in hydrodynamical simulations.

2. Event-by-event fluctuations might be of similar magnitude in quantities like the spatial and momentum anisotropy but while they remain smooth functions of time in hydrodynamics significant variations are observed within in a single event in PHSD as a function of time (Fig. 1).

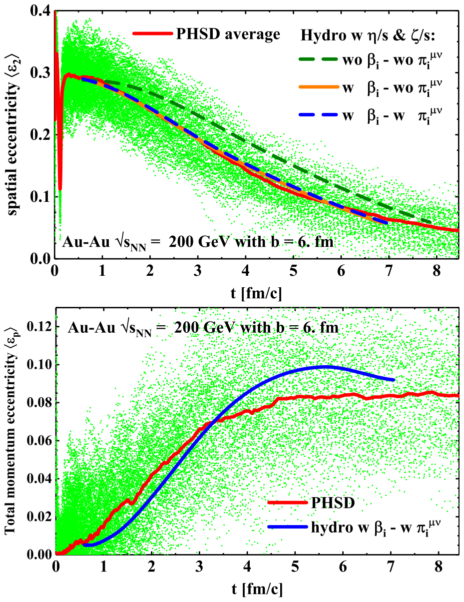

Figure 1: (Color online) Event-by-event averaged spatial eccentricity ϵ_2 of 100 PHSD events and 100 VISHNU events with respect to proper time, for a peripheral Au+Au collision ($b = 6$ fm) at $\sqrt{s_{NN}} = 200$ GeV. The green dots show the distribution of each of the 100 PHSD events used in this analysis. The solid red line is the average over all the green dots. (Top) The green, orange and blue lines correspond to hydrodynamical evolution taking different initial condition scenarios. (Bottom) The blue line corresponds to the standard hydrodynamical evolution taking the 100 initial conditions which are generated from PHSD events.

References

[1] Y. Xu, P. Moreau, T. Song, M. Nahrgang, S. A. Bass and E. Bratkovskaya, arXiv:1703.09178 [nucl-th].

[2] W. Cassing and E. L. Bratkovskaya, Phys. Rev. C **78**, 034919 (2008).

[3] W. Cassing and E.L. Bratkovskaya, Nucl. Phys. A **831**, 215 (2009).

[4] E. L. Bratkovskaya, W. Cassing, V. P. Konchakovski and O. Linnyk, Nucl. Phys. A **856**, 162 (2011).

[5] H. Song and U. W. Heinz, Phys. Rev. C **77**, 064901 (2008).

[6] C. Shen, Z. Qiu, H. Song, J. Bernhard, S. Bass and U. Heinz, Comput. Phys. Commun. **199**, 61 (2016).

---

* This work in part was supported by the LOEWE center HIC for FAIR and the HGS-HIRe as well as by BMBF and DAAD. The computational resources have been provided by the LOEWE-CSC. SAB, MG and YX acknowledge support by the U.S. Department of Energy under grant no. DE-FG02-05ER41367.

Particle production in nucleus-nucleus collisions at SIS energies*

Vinzent Steinberg[1,2], *Dmytro Oliinychenko*[1,3], *and Hannah Petersen*[1,2,4]

[1]Frankfurt Institute for Advanced Studies, Frankfurt am Main, Germany; [2]Institute for Theoretical Physics, Goethe University Frankfurt, Germany; [3]Bogolyubov Institute for Theoretical Physics, Kiev, Ukraine; [4]GSI, Darmstadt, Germany

In this report some results for particle production in heavy-ion reactions at $E_{\text{kin}} = 0.4 - 2A\,\text{GeV}$ with a new microscopic, hadronic transport approach SMASH (Simulating Many Accelerated Strongly-interacting Hadrons) [1] are shown.

56 mesons and 60 baryons (+ anti particles) are implemented in the model and can perform $2 \leftrightarrow 2$ and $2 \leftrightarrow 1$ reactions using the geometric collision criterion, effectively solving the relativistic Boltzmann equation. In SMASH, particle production in nucleus-nucleus collisions mainly happens via $NN \rightarrow NR, RR$ with subsequent decays of the formed resonances R. To test that resonances are implemented correctly, the elementary cross sections are compared to experimental data and detailed balance in an equilibrated box is verified.

To be able to compare to experimental data from heavy-ion collisions, it is necessary to implement additional physics. The effects of these features can be seen in Figure 1: Soft nucleon-nucleon potentials (Skyrme and symmetry) decrease the pion multiplicity while Fermi motion increases it significantly. Pauli blocking inhibits some reactions, resulting in a slightly lower multiplicity. In the end, the total pion multiplicity is overestimated (similar to some other transport models), but the ratio agrees rather well with the FOPI measurements. Only at the lowest energies the ratio is influenced by Fermi motion, potentials and Pauli blocking.

This shows that heavy-ion collisions at SIS energies can be reasonably well described with the resonance approach. However, to extend SMASH to higher energies relevant for FAIR, it is necessary to model the cross sections with a different approach. Future work includes integrating string fragmentation into SMASH by using PYTHIA [3] and exploring effective many-particle interactions via forced thermalization [4].

References

[1] J. Weil *et al.*, Phys. Rev. C **94** (2016) no.5, 054905. doi:10.1103/PhysRevC.94.054905

[2] W. Reisdorf *et al.* [FOPI Collaboration], Nucl. Phys. A **781** (2007) 459 doi:10.1016/j.nuclphysa.2006.10.085

[3] T. Sjöstrand *et al.*, Comput. Phys. Commun. **191**, 159 (2015) doi:10.1016/j.cpc.2015.01.024

[4] D. Oliinychenko and H. Petersen, J. Phys. Conf. Ser. **832** (2017) no.1, 012052. doi:10.1088/1742-6596/832/1/012052

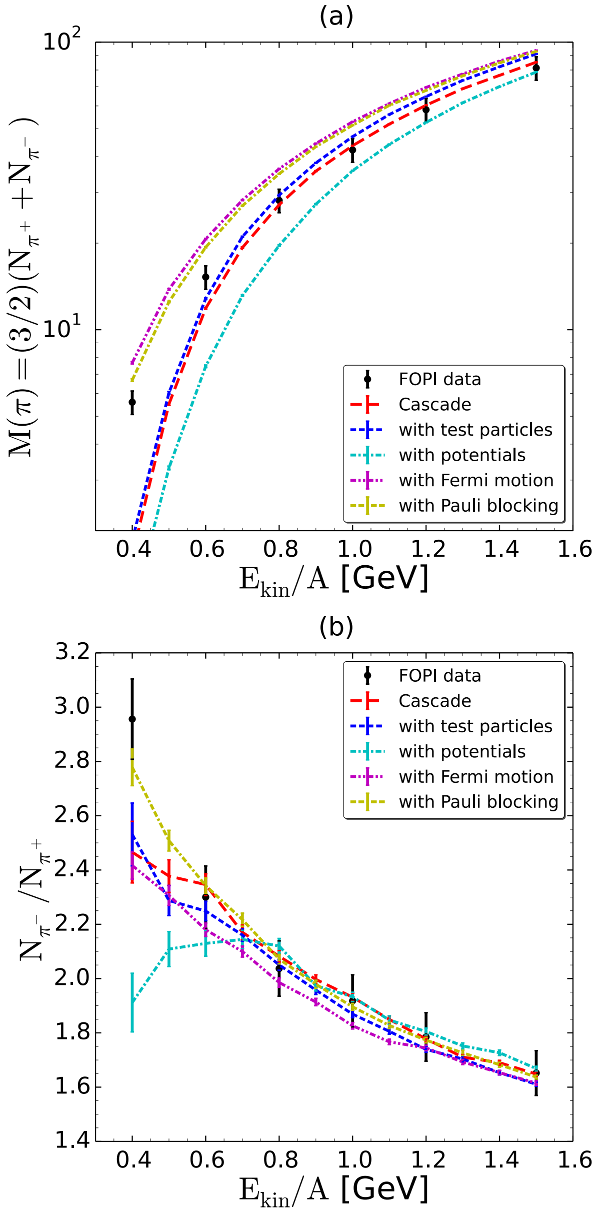

Figure 1: Pion production in gold-gold collisions at kinetic energies ranging from $0.4A\,\text{GeV}$ to $1.6A\,\text{GeV}$, as measured by FOPI [2] (markers), in comparison to SMASH (lines). Plot (a) shows the excitation function of π^+ and π^- multiplicities, plot (b) shows the ratio. The following features are successively switched on: 20 test particles per real particle, Skyrme and symmetry potentials, Fermi motion, Pauli blocking.

---

* Work supported by GSI and the Helmholtz Association with the Helmholtz Young Investigator Group VH-NG-822, HIC for FAIR, LOEWE, HGS-HIRe, and the Deutsche Telekom Stiftung

DOI:10.15120/GR-2017-1

$K^*/\bar{K}^*$ dynamics in the nuclear medium*

Andrej Ilner[†1,2], *Daniel Cabrera*[‡1,2], *Christina Markert*[§3], *and Elena Bratkovskaya*[¶1,2]
[1]Frankfurt Institute for Advanced Studies, Ruth-Moufang-Straße 1, 60438 Frankfurt am Main, Germany; [2]Institut für theoretische Physik, Johann Wolfgang Goethe-Universität, Max-von-Laue-Straße 1, 60438 Frankfurt am Main, Germany; [3]The University of Texas at Austin, Physics Department, Austin, Texas, USA

We study the in-medium properties and dynamics of the vector-mesons $K^*/\bar{K}^*$ in a dense and hot nuclear medium within the Parton-Hadron-String Dynamics (PHSD) transport approach. By $K^*/\bar{K}^*$ we are referring to all of the isospin channels, i.e. $K^* = [K^{*+}, K^{*0}]$ (vector mesons with a $\bar{s}$ and a u and d quark, respectively) and $\bar{K}^* = [K^{*-}, \bar{K}^{*0}]$ (vector mesons with a s and a d and u quark respectively). The in-medium properties of the $K^*/\bar{K}^*$ have been calculated on the basis of the G-Matrix approach, a unitary self-consistent chiral model, as complex self-energies and have been implemented in PHSD in the form of density- and temperature-dependent widths and effective masses through the relativistic Breit-Wigner spectral function, defined as

$$A_V\left(M,\rho_N\right) = \frac{\frac{2}{\pi}\cdot C_1\cdot M^2\cdot\Gamma_V^*\left(M,\rho_N\right)}{\left(M^2 - {M_V^*}^2\left(\rho_N\right)\right)^2 + \left(M\Gamma_V^*\left(M,\rho_N\right)\right)^2}. \tag{1}$$

The invariant mass of the meson $V = [K^*, \bar{K}^*]$ is denoted as M, ρ_N is the nuclear baryon density and C_1 is a normalisation constant which is determined through the normalisation of the spectral function, i.e. $\int_0^\infty A_V\left(M,\rho_N\right)\, dM = 1$.

The G-Matrix specral function contains the in-medium properties of the $K^*/\bar{K}^*$ in terms of the complex self-energy obtained by solving the Bethe-Salpeter equation. We can relate the real and imaginary parts of the self-energy to the width and the mass shift of the Breit-Wigner spectral function such that the real part of the self-energy is related to the mass shift

$$\mathrm{Re}\left(\Pi_i\left(M_V^*,\rho_N\right)\right) = M_V^2 - \left(M_V^*\right)^2, \tag{2}$$

whereas $M_V = M_{K^*/\bar{K}^*} = 0.892$ GeV is the vacuum mass of the $K^*/\bar{K}^*$ meson, and the imaginary part of the self-energy to the width

$$\mathrm{Im}\left(\Pi_V\left(M,\rho_N\right)\right) = -\Gamma_V^*\left(M,\rho_N\right)\cdot M \tag{3}$$

with a vacuum width for the $K^*/\bar{K}^*$ of $\Gamma_V^0 = 42$ MeV.

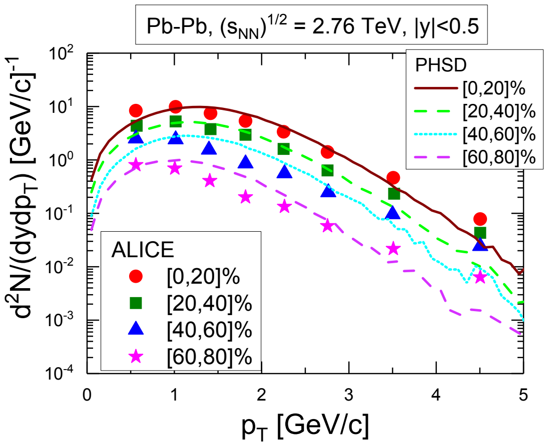

Figure 1: The transverse momentum spectrum $d^2N/\left(dydp_T\right)$ is shown at midrapidity for a PbPb collision at a centre of mass energy of $\sqrt{s_{NN}} = 2.76$ TeV for different centralities. The lines show results from PHSD while the symbols show data from ALICE [3].

The spectral function was implemented into PHSD in the form of cross sections for the $K^*\bar{K}^*$ and also in the hadronisation process of the quarks [1]. Experimental data from RHIC can be described very successfuly within PHSD and the implemented $K^*\bar{K}^*$ in-medium effects for pp and AuAu collisions at different centralities. However, we found a sizable difference between the spectra as taken from the decay point of the $K^*\bar{K}^*$ and the spectra as reconstructed from the final kaon and pion pairs [2]. Furthermore, we have performed additional studies within PHSD and $K^*/\bar{K}^*$ in-medium effects at higher and lower energies. In figure 1 the p_T spectrum for a PbPb collision at LHC can be seen. PHSD describes these data very well, if the final $K\pi$ pairs are taken and experimental cuts to the invariant mass spectrum are taken into account. However, just like for RHIC [2], we find that this spectrum differs from the measured spectrum at the $K^*/\bar{K}^*$ decay point, i.e. the spectrum is lower and softer.

References

[1] A. Ilner, D. Cabrera, P. Srisawad and E. Bratkovskaya, Nucl. Phys. A **927** (2014) 249

[2] A. Ilner, D. Cabrera, C. Markert and E. Bratkovskaya, Phys. Rev. C **95** (2017) no.1, 014903

[3] B. B. Abelev *et al.* [ALICE Collaboration], Phys. Rev. C **91** (2015) 024609

---

[*] Work supported by the Helmholtz International Center for FAIR within the framework of the LOEWE program. A.I. acknowledges support by GSI, HGS-HIRe for FAIR and H-QM. D.C. acknowledges support by BMBF (Germany).

[†] ilner@fias.uni-frankfurt.de
[‡] cabrera@fias.uni-frankfurt.de
[§] cmarkert@physics.utexas.edu
[¶] Elena.Bratkovskaya@th.physik.uni-frankfurt.de

DOI:10.15120/GR-2017-1

Dilepton production in proton-proton collisions in comparison to HADES measurements*

J. Staudenmaier[†2,3], *J. Weil*[2], *and H. Petersen*[1,2,3]

[1]GSI, Darmstadt, Germany; [2]Frankfurt Institute for Advanced Studies (FIAS), Frankfurt am Main, Germany; [3]Johann Wolfgang Goethe-Universität, Frankfurt am Main, Germany

Lepton pairs are clean probes for strongly-interacting matter, since they only interact electromagnetically. They are directly emitted from the hot and dense medium created in a heavy-ion collision, whereas hadronic probes are rescattered or absorbed. It is therefore possible to extract medium properties and medium modifications of resonances from dileptons over the whole lifetime of such collisions. Dileptons are measured for low beam energies by the HADES collaboration at GSI [1].

Describing heavy-ion collisions theoretically remains challenging, since no calculation from first principles is able to model strongly-interacting many-body systems. Therefore an effective model based on the relativistic Boltzmann equation is used in this work. SMASH (=Simulating Many Accelerated Strongly-interacting Hadrons) is a new hadronic transport approach, which has been developed with the intention to provide a standard reference for hadronic systems with vacuum properties [2].

The approach describes all resonances with dilepton decays which are relevant in the low invariant mass region. Dileptons in SMASH [3] are produced by decays either through direct decays of the vector mesons ρ, ω and ϕ or through Dalitz decays from the pseudoscalar mesons π^0 and η or the ω and Δ resonances. In order to obtain better statistics the so called *Time-Integration-Method* or also called *Shining-Method* [3] is used.

Figure 1 shows the di-electron invariant mass spectrum for proton-proton collisions at a kinetic energy of 3.5 GeV. The thick black line represents the total dilepton contribution, which is the sum of all the different decay contributions (coloured lines). The spectrum looks qualitatively as expected. The invariant mass region below 400 MeV is dominated by the Dalitz decays of the pseudoscalar mesons π^0 and η, whereas in the invariant mass region above 400 MeV the vector mesons ρ and ω are dominant. Since those are direct decays, features of the resonance properties, e.g. the width, can be seen. The ω has a much smaller width and therefore also the sharper peak in the dilepton spectrum compared to the ρ meson, which has a very broad peak structure. The Dalitz decays of the ω and the Δ resonances also contribute to the total spectrum, but are always smaller than the dominant yields.

Also plotted in Figure 1 in order to compare with experimental results is data from HADES [1]. The overall agreement with the data is good, which not only validates the dilepton production, but also the description of hadronic resonances within SMASH. In particular the lower invariant mass region is in good agreement. However, it is important to note that there is tension with the data in the vector meson dominated region. The data hints at a ϕ peak around 1 GeV, which is lacking in SMASH, since no ϕ mesons are produced in elementary collisions yet. Furthermore, the total yield overshoots the data in the region below and above the ω peak. Both can be attributed to a high ρ yield in these regions, which needs further investigation. One possibility are overestimations of the branching ratios of baryonic resonances (N^*, Δ^*) decaying into ρ mesons. New results [5] report substantial lower branching ratios, which would decrease the ρ yield in the relevant region.

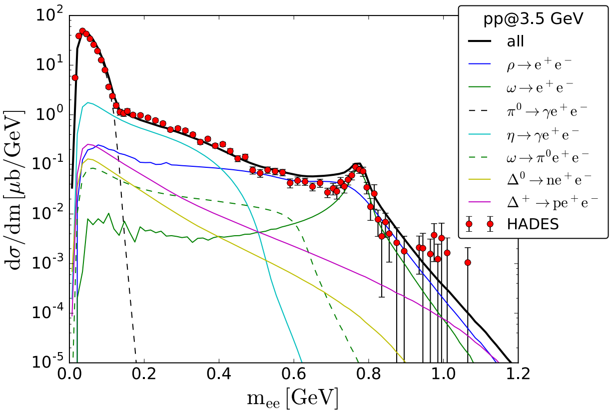

Figure 1: Invariant mass spectrum of di-electrons produced by pp collisions at $E_{kin} = 3.5$ GeV compared to HADES data from [1].

References

[1] Agakishiev G et al (HADES), Eur. Phys. J. A48 (2012) 64

[2] Weil J et al, Phys.Rev. C94 (2016) no.5, 054905

[3] Staudenmaier J et al, J.Phys.Conf.Ser. 832 (2017) no.1, 012037

[4] Schmidt K et al, Phys. Rev. C79 /2009) 064908

[5] Agakishiev G et al (HADES), Eur. Phys. J. A 50 (2014) 82

---

[*] Work supported by Helmholtz Nachwuchsgruppe VH-NG-822, by the LOEWE Initiative HIC for FAIR of the State of Hesse and GSI. Computational resources have been provided by the Center for Scientific Computing (CSC) at the Goethe- University of Frankfurt.

[†] staudenmaier@fias.uni-frankfurt.de

DOI:10.15120/GR-2017-1

The production of primordial J/ψ in p+p and relativistic heavy-ion collisions[*]

T. Song[†][1,2,3], *E. Bratkovskaya*[2,4], *and J. Aichelin*[3,5]

[1]Universität Gießen, Germany; [2]Institute for Theoretical Physics, Johann Wolfgang Goethe Universität, Frankfurt am Main, Germany; [3]FIAS, Frankfurt am Main, Germany; [4]GSI, Darmstadt, Germany; [5]Subatech, Nantes Cedex 3, France

Quarkonium production is special in the respect that it includes both, perturbative and non-perturbative, processes, where the former corresponds to the production of a heavy quark pair and the latter to the formation of a bound state from the pair. Though the former process is well described by pQCD, the latter needs a model.

We show that charmoninum production in p+p collisions can be described by projecting the position and momentum of the charm and anticharm quarks onto the Wigner density of the charmonium. The energy and momenta of the initial charm and anticharm quarks are given by the PYTHIA event generator, which has been tuned to reproduce the FONLL calculations. The radius of each charmonium state is a parameter to fit the experimental data on the total yield of J/ψ as well as the feed-down from the excited states of charmonium. We show in Fig. 1 that the experimental data in p+p collisions at $\sqrt{s} = 200$ GeV and 2.76 TeV are reproduced with the rms radii of 0.5, 0.55, and 0.9 fm respectively for J/ψ $(1S)$, χ_c $(1P)$ and ψ' $(2S)$, which are close to those calculated in a potential model. The distinguished feature of our approach is that it takes into account the spatial information of charm and anti-charm quarks.

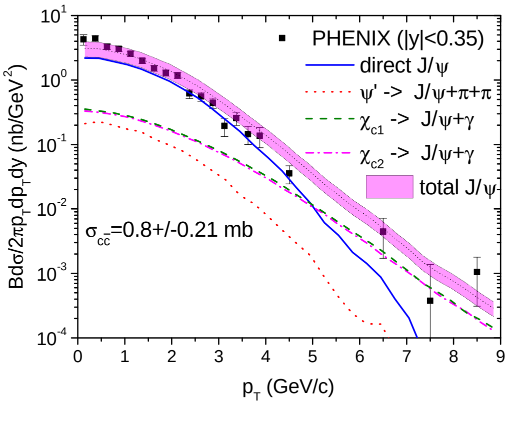

Figure 1: J/ψ production in p+p collisions at $\sqrt{s} = 200$ GeV including the feed-down from χ_c and ψ' in comparison with the experimental data from the PHENIX Collaboration [1].

While in p+p collisions mostly only one pair of charm quarks is produced, in relativistic heavy-ion collisions many charm quark pairs are produced in a small volume. Since many charm quark pairs are produced nearby in coordinate space, there is a probability for charm and anticharm quarks from two different initial pairs to form a charmonium. Using the same approach as in p+p collisions but allowing for the formation of charmonium from two different initial charm quark pairs, we find 46 % enhancement of primordial J/ψ in 0-20 % cental Au+Au collisions at $\sqrt{s} = 200$ GeV and an enhancement of a factor of 2.7 in 0-20 % cental Pb+Pb collisions at $\sqrt{s} = 2.76$ TeV, as shown by dotted line in Fig. 2.

The properties of charmonia change in the QGP matter produced in relativistic heavy-ion collisions. To estimate this effect we simply increase the radius by a factor of two and find that the production of primordial J/ψ reduces to 32 % in 0-20 % central Au+Au collisions at $\sqrt{s} = 200$ GeV, and to 86 % in 0-20 % central Pb+Pb collisions at $\sqrt{s} = 2.76$ TeV. It implies that the nuclear matter effects are important to describe J/ψ production in relativistic heavy-ion collisions.

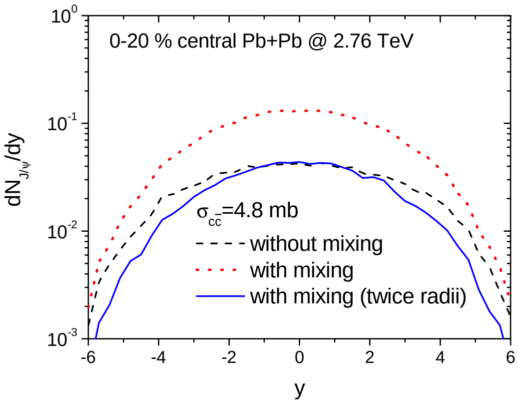

Figure 2: Rapidity distributions of J/ψ in $0-20$ % central Pb+Pb collisions at $\sqrt{s} = 2.76$ TeV. For the dashed curve the creation of charmonium from c and $\bar{c}$ from different initial collisions is excluded. For the dotted line we do not exclude this mixing. The solid lines show calculations in which the Wigner density has been modified to simulate QGP effects.

References

[1] A. Adare and PHENIX Collaboration, "J/ψ production versus transverse momentum and rapidity in p^+p collisions at $\sqrt{s}$ = 200-GeV", Phys. Rev. Lett. **98** (2007) 232002.

---

[*] Work supported by HIC4FAIR/DFG.

[†] song@fias.uni-frankfurt.de

Numerical relativistic magneto-hydrodynamics for heavy ion collisions[*]

G. Inghirami[†][1,2,3,4], *L. Del Zanna*[5,6,7], *A. Beraudo*[8], *M. Haddadi Moghaddam*[9,8], *F. Becattini*[5,6], *and M. Bleicher*[1,2,3,4]

[1]FIAS, Frankfurt am Main, Germany; [2]Goethe-Universität, Frankfurt am Main, Germany; [3]GSI, Darmstadt, Germany; [4]J. von Neumann Institute for Computing, Jülich, Germany; [5]Università degli Studi di Firenze, Firenze, Italy; [6]INFN - Sezione di Firenze, Firenze, Italy; [7]INAF - Osservatorio di Arcetri, Firenze, Italy; [8]INFN - Sezione di Torino, Torino, Italy; [9]Hakim Sabzevari University, Sabzevar, Iran

In the context of heavy ion collisions, the huge magnetic fields ($e|\vec{B}| \approx 10\, m_{\pi_0}^2$) generated by the fast moving electric charges contained in the nuclei might produce many interesting phenomena, like the chiral magnetic effect [1], changes in the directed and elliptic flows of the emitted charged particles [2, 3], a modification of the QCD equation of state [4, 5] or a mass shift of the light mesons [6, 7]. We modified the ECHO-QGP code [8, 9] to include the effects of such strong magnetic fields into the hydrodynamical description of the expanding fireball created after the collision, in the limit of an infinite electrical conductivity of the fluid and adopting the massless particles equation of state $p = e/3$. We executed several tests to validate the code, then we performed a 2D+1 simulation of an Au+Au collision at $\sqrt{s_{NN}} = 200\,\mathrm{GeV}$ A. The initial energy distribution has been computed using the Glauber model with an impact parameter $b = 10\,\mathrm{fm}$, while the magnetic field has been initialized according to the model described in Ref.([10]), assuming that the electrical conductivity of the medium before starting the hydro evolution was $5.8\,\mathrm{MeV}$. The time evolution of the magnetic field at the center of the grid is shown in Fig.(1): due to the fluid expansion on the transverse plane, it decays a bit faster than in the case a pure Bjorken expansion, but still much slower than in the case of a magnetic field generated by particles freely streaming in the void. With these initial conditions, we did not appreciate any change in the elliptic flow of the charged pions, computed with the "standard" Cooper Frye prescription. However, more realistic and extensive simulations are needed before drawing any reasonable conclusion, e.g. 3D+1 runs with lattice QCD + hadron gas EoS, taking into account viscous effects and a finite electrical conductivity, at different collision energies, using more sophisticated methods to compute the initial conditions, varying the impact parameters and performing a final hadronic rescattering. The present work should be considered just a necessary, but still preliminary step toward a more complete magneto-hydrodynamical description of the quark-gluon plasma evolution in heavy ion collisions.

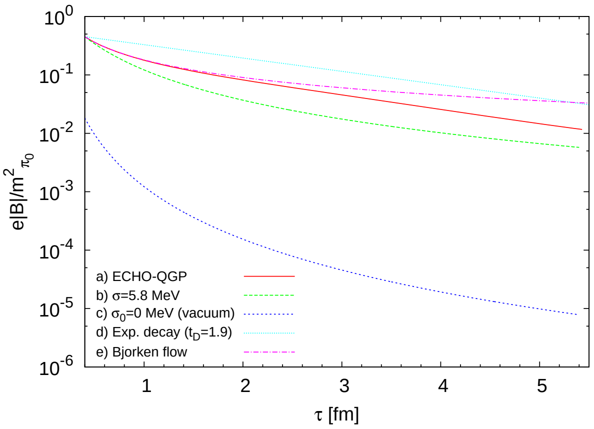

Figure 1: Comparison of the time evolution of the magnitude of the magnetic field (in neutral pion mass units squared) at the center of the grid. In the plot are depicted five different cases: a) ECHO-QGP, computing the initial $\vec{B}$ field assuming $\sigma = 5.8\,\mathrm{MeV}$ b) magnetic field generated by the electric charges of the two colliding nuclei moving in a medium with uniform and constant electrical conductivity $\sigma = 5.8\,\mathrm{MeV}$ c) same as in case b), but assuming zero electrical conductivity $\sigma = 0\,\mathrm{MeV}$ (vacuum) d) assuming an exponential decay of the magnetic field with a characteristic decay time $t_D = 1.9\,\mathrm{fm}$ e) Bjorken flow.

References

[1] K. Fukushima, D. E. Kharzeev and H. J. Warringa, Phys. Rev. D **78** (2008)

[2] U. Gursoy, D. Kharzeev and K. Rajagopal, Phys. Rev. C **89** (2014)

[3] G. S. Bali, F. Bruckmann, G. Endrodi, F. Gruber and A. Schaefer, JHEP **1304** (2013)

[4] G. S. Bali, F. Bruckmann, G. Endrödi, S. D. Katz and A. Schäfer, JHEP **1408** (2014)

[5] G. S. Bali *et al.*, JHEP **1202** (2012)

[6] J. O. Andersen, Phys. Rev. D **86** (2012)

[7] E. V. Luschevskaya and O. V. Larina, JETP Lett. **98** (2014)

[8] G. Inghirami, L. Del Zanna, A. Beraudo, M. H. Moghaddam, F. Becattini and M. Bleicher, Eur. Phys. J. C **76** (2016)

[9] L. Del Zanna *et al.*, Eur. Phys. J. C **73** (2013)

[10] K. Tuchin, Phys. Rev. C **88** (2013)

---

[*] G.Inghirami was supported by a GSI grant in cooperation with the John von Neumann Institute for Computing. G. Inghirami also gratefully acknowledges support from the H-QM and HGS-HIRe graduate schools. The computational resources were provided by the INFN-FI, by the FIAS and by the Center for Scientific Computing of the Goethe University. This work was also supported by the University of Florence grant "Fisica dei plasmi relativistici: teoria e applicazioni moderne".

[†] inghirami@fias.uni-frankfurt.de

Identifying QCD transition with deep learning [*]

L.-G. Pang[1,5], *K. Zhou*[1], *N. Su*[† 1], *H. Petersen*[1,2,3], *H. Stöcker*[1,2,3], *and X.-N. Wang*[4,5]

[1]Frankfurt Institute for Advanced Studies, 60438 Frankfurt am Main, Germany; [2]Institut für Theoretische Physik, Goethe Universität, 60438 Frankfurt am Main, Germany; [3]GSI Helmholtzzentrum für Schwerionenforschung, 64291 Darmstadt, Germany; [4]Key Laboratory of Quark and Lepton Physics (MOE) and Institute of Particle Physics, Central China Normal University, Wuhan, 430079, China; [5]Lawrence Berkeley National Laboratory, Berkeley, CA 94720, USA

Introduction

One primary goal of ultra-relativistic heavy-ion collision experiments – currently carried out at RHIC (BNL) and LHC (CERN), and the forthcoming one at FAIR (GSI) – is to study the QCD transition, which is conjectured to be a crossover at small density (and moderately high temperature), and 1st order at moderate density (and lower temperature), with a critical point separating the two. Although it is believed that strongly coupled QCD matter can be created in these collisions, a direct access to the bulk properties of the matter such as the equation of state (EoS) and transport coefficients is impossible due to the highly dynamical nature of the collisions. What directly measured in experiments are the final-state particle spectra $\rho(p_T, \Phi)$, where p_T is the transverse momentum and Φ is the azimuthal angle of the final charged hadrons. So far, there has been no establishment of noticeable and unique correspondence between $\rho(p_T, \Phi)$ and the bulk properties during the evolution, which has thus posed a pressing challenge in testing the non-perturbative nature of QCD for the high-energy-physics community.

Deep learning is one branch of machine learning, which aims at understanding high-level representations of data using a deeper structure of multiple processing layers. Its features suggest that it could be adopted to uncover hidden information from the highly implicit data of heavy-ion experiments. Here we review a recent exploratory study, which provided a first step in directly connecting QCD bulk properties and raw data of heavy-ion collisions using state-of-the-art deep-learning techniques [1].

Results and discussions

The evolution of strongly coupled QCD matter can be well described by 2nd-order dissipative hydrodynamics. The EoS of the medium is a crucial input in solving the hydrodynamic equations, and the nature of the QCD transition (crossover or 1st order) strongly affects the hydrodynamic evolution. The final $\rho(p_T, \Phi)$ are obtained from the Cooper-Frye formula for particle i at mid-rapidity

$$\rho(p_T, \Phi) \equiv \frac{dN_i}{dY p_T dp_T d\Phi} = g_i \int_\sigma p^\mu d\sigma_\mu f_i \,, \qquad (1)$$

where N_i is the particle number density, Y is the rapidity, g_i is the degeneracy, $d\sigma_\mu$ is the freeze-out hypersurface element, f_i is the thermal distribution.

We found unique encoders of the EoS inside $\rho(p_T, \Phi)$ in terms of high-level representations using deep-learning techniques, which are not captured by conventional observables. This was achieved by constructing a convolutional neural network (CNN) and supervisedly training it with labeled $\rho(p_T, \Phi)$ of charged pions generated by the event-by-event hydrodynamic package CLVisc [2] with two different EoSs as input: crossover and 1st order. We then used $\rho(p_T, \Phi)$ generated by independent simulations (CLVisc with different setup parameters and another hydrodynamic package iEBE-VISHNU [3]) for testing. The performance of our method is surprisingly robust against other simulation parameters and an overall $\gtrsim 97\%$ testing accuracy was obtained, see Tab. 1 for the testing results and please check Ref. [1] for further details.

TESTING RESULTS	GROUP 1		GROUP 2	
	EOSL	EOSQ	EOSL	EOSQ
Number of Events	3349	3994	4164	4752
Accuracies	98.5%	91.6%	99.2%	99.2%

Table 1: Testing accuracies for two groups (iEBE-VISHNU and CLVisc with the IP-Glasma-like initial condition) of the testing dataset.

Our method yields a novel perspective on identifying the nature of the QCD transition in heavy-ion collisions. By adopting deep CNNs, we firmly demonstrated that discriminative and traceable projections – "encoders" – from the QCD transition onto the experimentally direct accessible $\rho(p_T, \Phi)$ do exist in the complex and highly dynamical heavy-ion collisions. The deep CNN provides a powerful and efficient "decoder" from which the EoS information can be extracted directly from the $\rho(p_T, \Phi)$. In this way, the high-level representations, which help decoding the EoS information in our method, act as an "EoS-meter" for the QCD matter created in heavy-ion collisions. Our study might provide a key to the experimental determination of QCD EoS and search for the critical end point.

References

[1] L.-G. Pang, K. Zhou, N. Su, H. Petersen, H. Stöcker, and X.-N. Wang, arXiv:1612.04262 [hep-ph].

[2] L.-G. Pang, Q. Wang, and X.-N. Wang, Phys. Rev. C **86**, 024911 (2012).

[3] C. Shen, Z. Qiu, H. Song, J. Bernhard, S. Bass, and U. Heinz, Comput. Phys. Commun. **199**, 61 (2016).

---

[*] Work supported in part by GSI.

[†] nansu@fias.uni-frankfurt.de

DOI:10.15120/GR-2017-1

Higher-order baryon number susceptibilities: interplay between the chiral and the nuclear liquid-gas transitions*

J. Steinheimer[†1], *A. Mukherjee*[1,2], *and S. Schramm*[1,2]

[1]Frankfurt Institute for Advanced Studies, Ruth-Moufang-Straße 1, D-60438 Frankfurt am Main, Germany; [2]Institut für Theoretische Physik, Goethe Universität Frankfurt, Max-von-Laue-Straße 1, D-60438 Frankfurt am Main, Germany

Theoretical studies employing lattice QCD methods have already established that the transition from hadrons to quarks proceeds as a smooth crossover in the case of vanishing net baryon number density [1, 2]. For finite net baryon density, the use of standard lattice QCD methods is limited by the so-called fermion sign problem. One proposed universal characteristic of a possible critical point of QCD is that higher-order fluctuation moments of observables diverge, at least for an infinite system size and relaxation time [3, 4]. We use an improved version of the SU(3) flavor parity-doublet quark-hadron model to investigate the higher order baryon number susceptibilities near the chiral and the nuclear liquid-gas transitions. We observe a strong interplay between the chiral and liquid-gas transition at intermediate baryo chemical potentials [5].

Model Description

We use the so called Quark-Hadron Chiral Parity Doublet Model (QχP) for a consistent description of strongly interacting matter which undergoes a chiral and deconfinement transition. The model parameters can be chosen so the model gives a good description of nuclear ground state and compact star properties as well as zero baryon density lattice QCD data. For a detailed description see [5]. Figure 1 shows the resulting phase diagram with both the nuclear liquid-gas transition and the chiral transition as function of T and μ_B.

To quantify the effect of the liquid-gas transition on the net-baryon susceptibilities we extract the cumulant ratio χ_4/χ_2 as function of the beam energy, using the freeze out curve obtained from a thermal fit to particle multiplicities [6], shown in figure 2.

In summary we have found that the interplay between liquid-gas and chiral transition has an effect on the equation of state and the extracted susceptibilities in a significant range of the phase diagram. This means that the influence of dense nuclear matter on the phase structure, even at large temperatures and moderate chemical potentials, cannot be neglected.

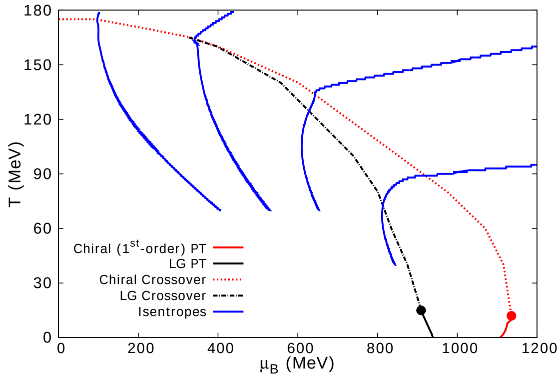

Figure 1: T-μ_B diagram showing the 1st-order liquid-gas (LG) phase transition (bold, black line), the 1st-order, chiral phase transition (bold, red line), the LG crossover (dashed, black line), the chiral crossover (dashed, red line), the LG Critical Point (black dot), the chiral Critical Point (red dot). Lines of constant entropy per baryon are shown as blue solid lines.

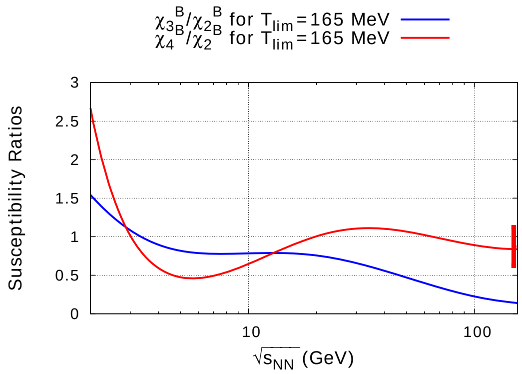

Figure 2: Susceptibility ratios as function of beam energy along the freeze-out line with $T_{\rm lim}$ = 165 MeV; with the value of χ_4^B/χ_2^B for $\mu_B \approx 0$, obtained from lattice data [7], represented by the thick, red bar.

References

[1] S. Borsanyi *et al.*, JHEP **1011**, 077 (2010)

[2] A. Bazavov and P. Petreczky [HotQCD collaboration], J. Phys. Conf. Ser. **230**, 012014 (2010)

[3] M. A. Stephanov, Phys. Rev. Lett. **102**, 032301 (2009)

[4] M. A. Stephanov, K. Rajagopal and E. V. Shuryak, Phys. Rev. Lett. **81**, 4816 (1998)

[5] A. Mukherjee, J. Steinheimer and S. Schramm, arXiv:1611.10144 [nucl-th].

[6] A. Andronic, P. Braun-Munzinger and J. Stachel, Phys. Lett. B **673**, 142 (2009) [Erratum-ibid. B **678**, 516 (2009)]

[7] R. Bellwied, S. Borsanyi, Z. Fodor, S. D. Katz and C. Ratti, Phys. Rev. Lett. **111**, 202302 (2013).

---

[*] Work supported by GSI, BMBF, HIC4FAIR and HGShire.

[†] steinheimer@fias.uni-frankfurt.de

DOI:10.15120/GR-2017-1

Van der Waals interactions in hadron resonance gas: from nuclear matter to lattice QCD

V. Vovchenko[1,2,3], *M.I. Gorenstein*[2,4], *and H. Stoecker*[1,2,5]

[1]ITP, Goethe University, Frankfurt, Germany; [2]FIAS, Frankfurt, Germany; [3]Taras Shevchenko University, Kiev, Ukraine; [4]BITP, Kiev, Ukraine; [5]GSI, Darmstadt, Germany

Extension of the ideal hadron resonance gas (Id-HRG) model is constructed which includes attractive and repulsive van der Waals (VDW) interactions between hadrons [1]. The model employs a novel multi-component quantum statistical VDW approach which incorporates the Fermi-Dirac and Bose-Einstein effects in the system of interacting particles [2]. In the present minimalistic setup we include the VDW interactions for all baryon-baryon and all antibaryon-antibaryon pairs. At the same time, the VDW interactions between all other hadron pairs are explicitly omitted. The VDW parameters of baryon-baryon interaction are assumed to be the same for all baryon pairs, and are fixed by the ground state properties of nuclear matter ($a \simeq 329$ MeV fm^3 and $b \simeq 3.42$ fm^3). This VDW-HRG model yields the nuclear liquid-gas transition at low temperatures and high baryonic densities with a critical point located at $T_c \simeq 19.7$ MeV and $\mu_c \simeq 908$ MeV ($n_c \simeq 0.07$ fm$^3 = 0.45\,n_0$).

The predictions of the model are confronted with the lattice QCD calculations at zero chemical potential. The inclusion of the VDW interactions between baryons does not spoil the existing agreement of the Id-HRG model with lattice data on the pressure and energy density, and it leads to an improved description of the speed of sound. Moreover, the VDW interactions lead to a qualitatively different behavior of cumulants of fluctuations of conserved charges, for many observables closely resembling the lattice QCD results. For instance, the VDW-HRG model predicts the drop of the χ_4^B/χ_2^B cumulant ratio for the net baryon number fluctuations in the crossover region, which is also seen on the lattice (see Fig. 1). The VDW interactions are found to have a substantial influence on the higher orders of fluctuations of conserved charges at finite chemical potential, in the regions where chemical freeze-out in heavy-ion collisions is expected to occur. For example, the region of negative χ_4^B/χ_2^B at small μ_B is smoothly connected to the region of the liquid-vapor phase transition in nuclear matter (Fig. 2), and seems relevant for "chemical freeze-out" in heavy-ion collisions (see dashed line). Thus, the nuclear liquid-gas transition manifests itself into non-trivial net-baryon fluctuations in heavy-ion collisions.

These results hint towards crucial importance of the VDW interactions in the hadron gas, and indicate that commonly performed comparisons of the Id-HRG model with the lattice data may result in misleading conclusions. In particular, our results suggest that hadrons do not melt quickly with increasing temperature, as one could conclude on the basis of the Id-HRG model analysis.

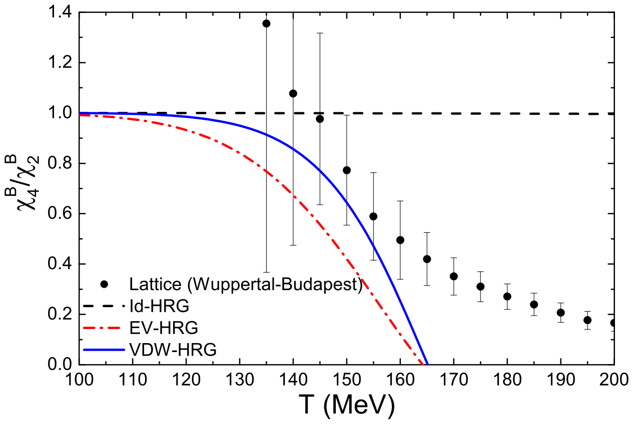

Figure 1: The temperature dependence of the χ_4^B/χ_2^B cumulant ratio for the net baryon number fluctuations. Calculations are done within the Id-HRG model (dashed lines), EV-HRG model with $b = 3.42$ fm^3 (dash-dotted lines), and VDW-HRG model with $b = 3.42$ fm^3 and $a = 329$ MeV fm^3 (solid lines). The lattice QCD results of the Wuppertal-Budapest collaboration [3] are shown by symbols.

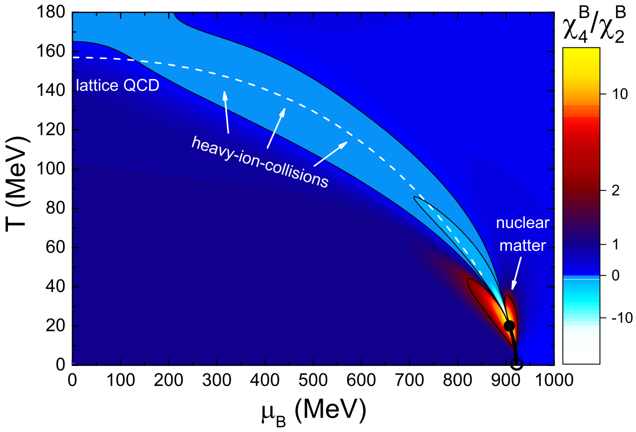

Figure 2: The χ_4^B/χ_2^B ratio calculated in the VDW-HRG model is exhibited in the T-μ_B plane.

References

[1] V. Vovchenko, M. I. Gorenstein, and H. Stoecker, Phys. Rev. Lett. **118**, 182301 (2017).

[2] V. Vovchenko, D. V. Anchishkin, and M. I. Gorenstein, Phys. Rev. C **91** (2015) 064314.

[3] R. Bellwied, S. Borsanyi, Z. Fodor, S. D. Katz, A. Pasztor, C. Ratti, and K. K. Szabo, Phys. Rev. D **92** (2015) 114505.

DOI:10.15120/GR-2017-1

New scenarios for hard-core interactions in a hadron resonance gas

L. M. Satarov[*][1,2], *V. Vovchenko*[1,3,4], *P. Alba*[1], *M. I. Gorenstein*[1,5], *and H. Stoecker*[1,3,6]
[1]FIAS, Frankfurt am Main; [2]Kurchatov Institute, Moscow; [3]Goethe University, Frankfurt am Main;
[4]Taras Shevchenko University, Kiev; [5]BITP, Kiev; [6]GSI, Darmstadt

To describe realistically the equation of state (EoS) of a hot and dense hadronic matter, one should take into account finite sizes of hadrons. In Ref. [1] we investigate thermodynamic properties of a hadron resonance gas (HRG) with a hard-core repulsion of particles. It is assumed that that hard core radii of all baryons (B) and antibaryons ($\overline{B}$) are equal (below they are denoted by r_B), but mesons (M) are point-like. In the Boltzmann approximation, introducing the excluded volume corrections one can write the following relation for the pressure P of HRG [2]:

$$P = T\left[\frac{n_M}{1-\eta} + \frac{n_B + n_{\overline{B}}}{1-4\eta}\right]. \qquad (1)$$

Here T is temperature, $n_M, n_B, n_{\overline{B}}$ are total densities of mesons, baryons, and antibaryons, respectively. The packing fraction $\eta = (n_B + n_{\overline{B}})\,v$ is proportional to the hard-core volume of a single (anti)baryon $v = 4\pi r_B^3/3$. The calculation are done for the baryon-symmetric case $n_{\overline{B}} = n_B$.

The conditions of chemical equilibrium lead to the transcendental equation for $n_B = n_B(T)$. By solving this equation one obtains partial densities of different hadrons at given T. We found that the equilibrium nucleon to pion ratio is a nonmonotonic function of T with a maximum in the temperature range $170 - 200$ MeV at $r_B = 0.3 - 0.5$ fm. This explains the appearance of the second high-temperature minimum of χ^2 obtained from the thermal fit of ALICE data in Ref. [3].

The above model (CI) assumes that the BB and $B\overline{B}$ interaction are the same and mesons do not penetrate into hard cores of (anti)baryons. We also consider two other scenarios: CII where antibaryons do not interact with baryons, and CIII where the $B\overline{B}$, MB and $M\overline{B}$ interactions are neglected. The EoS in the CII model is obtained by replacing $\eta \to n_B v = n_{\overline{B}} v$ in the second term of (1). In the CIII scenario, one should additionally omit the denominator in the first term. At fixed r_B the N/π ratio increases in the transition from CI to CII, and from CII to CIII.

We performed the fit of midrapidity yields of hadrons measured by the ALICE collaboration in the central Pb+Pb collisions at $\sqrt{s_{NN}} = 2.76$ TeV. This was done for the ideal HRG as well as for the CI, CII and CIII models. At each freeze-out temperature the system volume was determined by minimizing the χ^2 values of the fit.

The results for hard-core radii $r_B = 0.3 - 0.6$ fm are shown in Fig. 1. One can see that introducing the hard-core repulsion improves the fit quality. Also the structure of the $\chi^2/N_{\rm dof}$ curves is very different form the ideal gas case. As compared to the calculation with $r_B = 0$, the corresponding curves in the CI, CII and CIII models are noticeably wider and in many cases two minima appear. According to our results, omitting the meson-baryon and antibaryon-baryon interactions strongly influences the hadronic yields and their ratios.

This shows that extracting the chemical freeze-out temperature from the hadron yield data is a rather delicate and model-dependent procedure. The improved excluded volume calculations should take into account the difference between the BB and $B\overline{B}$ interactions.

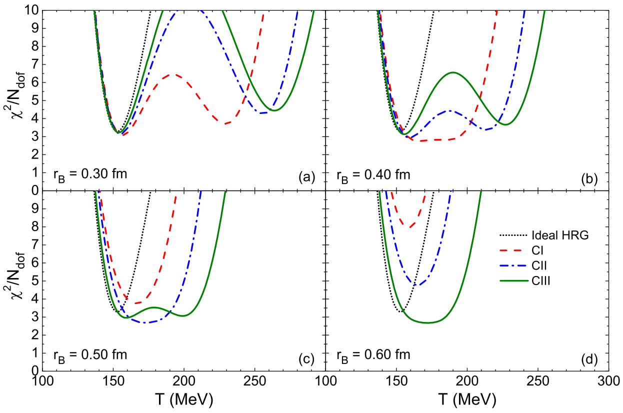

Figure 1: The temperature dependence of χ^2/N_{dof} for fitting the ALICE data on hadron yields in 0-5% central Pb+Pb collisions at $\sqrt{s_{NN}} = 2.76$ TeV. The dashed, dash-dotted, and solid curves correspond, respectively, to the models CI, CII, and CIII. The dotted lines are calculated in the ideal gas limit $r_B = 0$.

References

[1] L. M. Satarov, V. Vovchenko, P. Alba, M. I. Gorenstein, H. Stoecker, Phys. Rev. C 95 (2017) 024902

[2] L.M. Satarov, K.A. Bugaev, I.N. Mishustin, Phys. Rev. C 91 (2015) 055203

[3] V. Vovchenko, H. Stoecker, J. Phys. G 44 (2017) 055103; arXiv: 1512.08046 [hep-ph]

---

[*] satarov@fias.uni-frankfurt.de

DOI:10.15120/GR-2017-1

Effective size of glueballs in Yang-Mills theory[*]

P. Alba[†1], *W.M. Alberico*[2], *A. Nada*[2], *M. Panero*[2], *and H. Stöcker*[1,3,4]
[1]FIAS, Frankfurt am Main, Germany; [2]University of Turin & INFN, Turin, Italy; [3]Goethe Universität Frankfurt, Frankfurt am Main, Germany; [4]GSI, Darmstadt, Germany

It is well known that the confined phase of QCD matter is well described by the standard version of the Hadron-Resonance Gas (HRG) model, which however neglects repulsive interactions among hadrons. These can be easily implemented in the model through an Excluded Volume (EV) approach, in which every hadron has an effective radius r_j. In order to crosscheck the results found in the fit to particle yields [1], here we analyze the interaction measure for SU(2) and SU(3) Yang-Mills theories calculated by means of Monte-Carlo lattice simulations [2,3]. The pure gauge sector is a good benchmark, since here we have only one physical scale, much lower computational costs, and none of the problems related to the implementation of fermionic fields; in particular in SU(2) there is no ambiguity in the definition of the Hagedorn temperature T_H with respect to the critical temperature T_c.
In figure 1 we show the HRG calculations in comparison to the lattice results; it is clear how the introduction of EV effects drastically reduces the reduced χ^2, table 1 and table 2, giving a consistent description between the two theories, with the radius of the lightest glueball r_0 in the ballpark of 0.5-0.9 fm depending on the EV scheme.

	r_0 (fm)	Δr_0 (fm)	χ^2_{red}
point-like	0	0	8.16
fixed radius	0.65	0.12	0.74
direct prop.	0.47	0.19	1.87
inverse prop.	0.82	0.14	0.39

Table 1: Best-fit results of lattice data for the SU(2) interaction measure, to the glueball-gas model with different EV scenarios.

	r_0 (fm)	Δr_0 (fm)	χ^2_{red}
point-like	0	0	84.3
fixed radius	0.73	0.08	2.33
direct prop.	0.55	0.07	5.41
inverse prop.	0.91	0.10	0.82

Table 2: Best-fit results of lattice data for the SU(3) interaction measure, to the glueball-gas model with different EV scenarios.

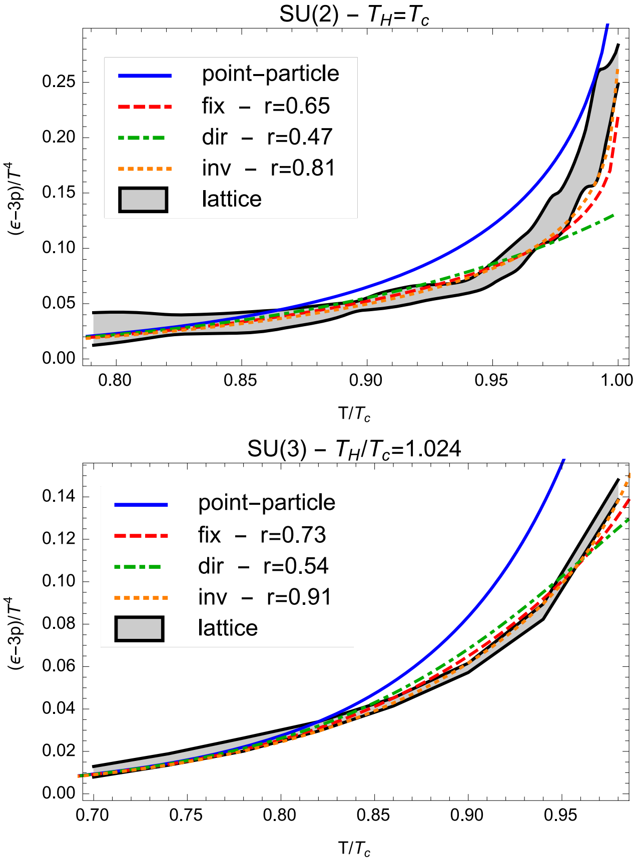

Figure 1: Interaction measure for SU(2) (upper panel) and SU(3) (lower panel) from lattice simulations [2,3] (band) and a gas of glueballs with the point-particle assumption (continuos line) and effective volume fixed (dashed), directly proportional (dot-dashed) and inversely proportional (dotted) to glueball masses.

References

[1] P. Alba, V. Vovchenko, M. I. Gorenstein and H. Stoecker, arXiv:1606.06542 [hep-ph].

[2] S. Borsanyi, G. Endrodi, Z. Fodor, S. D. Katz and K. K. Szabo, JHEP **1207**, 056 (2012) doi:10.1007/JHEP07(2012)056 [arXiv:1204.6184 [hep-lat]].

[3] P. Alba, W. M. Alberico, A. Nada, M. Panero and H. Stcker, arXiv:1611.05872 [hep-lat].

---

[*] This research is partially supported by HIC for FAIR within the LOEWE program of the state of Hesse.

[†] alba@fias.uni-frankfurt.de

Electromagnetic probes of a pure-glue initial state in nucleus-nucleus collisions at LHC energies

V. Vovchenko[1,2,3], *Iu. Karpenko*[4,5], *M.I. Gorenstein*[2,5], *L.M. Satarov*[2,6], *I.N. Mishustin*[2,6], *B. Kämpfer*[7,8], *and H. Stoecker*[1,2,9]

[1]ITP, Goethe University, Frankfurt am Main, Germany; [2]FIAS, Frankfurt am Main, Germany; [3]Taras Shevchenko University, Kiev, Ukraine; [4]INFN, Firenze, Italy; [5]BITP, Kiev, Ukraine; [6]Kurchatov Institute, Moscow, Russia; [7]HZDR, Dresden, Germany; [8]TU Dresden, Germany; [9]GSI, Darmstadt, Germany

Partonic matter produced in the early stage of ultrarelativistic nucleus-nucleus collisions is assumed to be composed mainly of gluons, while quarks and antiquarks are produced at later times. The implications of this chemical non-equilibrium scenario are studied within the ideal (2+1)–dimensional hydrodynamics with a time dependent (anti)quark fugacity [1]. We use the explicit parametrization for the quark fugacity, $\lambda(\tau) = 1 - \exp\left(\frac{\tau_0-\tau}{\tau_*}\right)$, where τ is the proper time, τ_* is the quark chemical equilibration time, τ_0 is the initial time of hydrodynamic evolution. The chemically equilibrium scenario ($\lambda = 1$) corresponds to the limit $\tau_* \to 0$. We use the equation of state which interpolates linearly between the lattice data for the purely gluonic Yang-Mills plasma and the lattice data for the (2+1)-flavor chemically equilibrated QCD matter. The modified vHLLE code [2] is used in numerical calculations.

We perform simulations for central Pb+Pb collisions at LHC energy of $\sqrt{s_{\rm NN}} = 2.76$ TeV. The initial energy density at $\tau_0 = 0.1$ fm/c is fixed to reproduce the hadronic observables in the chemical equilibrium ($\lambda = 1$) scenario. Figure 1 shows the density plot of the temperature in the coordinates (x, τ) for a simulation with $\tau_* = 5$ fm/c. The dashed curves correspond to $\tau_* = 0$. The chemically undersaturated matter is hotter as compared to the equilibrium case, which is a consequence of a reduced number of degrees of freedom in such a medium. A small region of first-order phase transition (FOPT) is also seen.

The spectra of electromagnetic probes – photons and dileptons – are also considered in the chemical non-equilibrium scenario. The QGP thermal photon emissions rates are modified by additional fugacity factors in undersaturated QGP. The calculated photon elliptic flow v_2^γ is exhibited in Fig. 2. In the chemical non-equilibrium scenario the momentum anisotropy of thermal photons is greatly enhanced at large p_T. The enhancement of the v_2^γ is also suggested by the preliminary data of the ALICE collaboration for direct photons [3]. The sensitivity of the results to chemical non-equilibrium effects, however, is greatly reduced when contributions from the prompt photons to the total direct photon spectrum are taken into account.

Stronger effects of are found for the thermal dilepton spectra, especially at large invariant masses $M \gtrsim 2$ GeV, where the deviations between two scenarios can reach one to two orders of magnitude. The corresponding experimental data are not available yet.

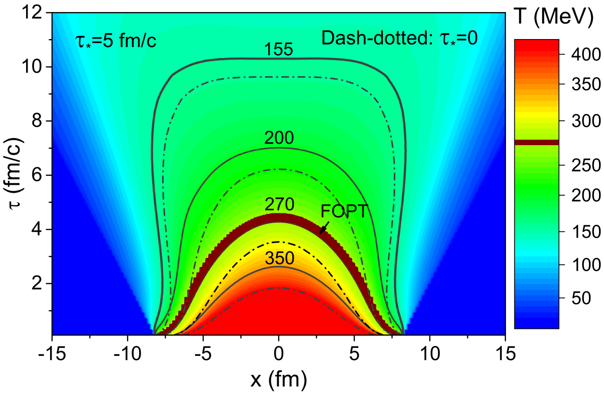

Figure 1: Contour plot of the temperature in the $x - \tau$ plane for the 0–20% most central Pb+Pb collisions at $\sqrt{s_{\rm NN}} = 2.76$ TeV for quark equilibration time $\tau_* = 5$ fm/c. The dash-dotted curves depict isotherms calculated for equilibrium matter with $\lambda = 1$.

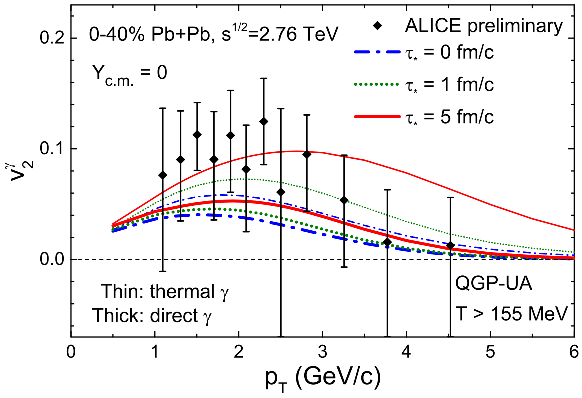

Figure 2: Elliptic flow v_2^γ of direct (thick lines) and thermal (thin lines) photons as a function of transverse momentum p_T in the $0 - 40\%$ central Pb+Pb collisions at $\sqrt{s_{\rm NN}} = 2.76$ TeV for different quark equilibration times τ_*. Experimental data are taken from Ref. [3].

References

[1] V. Vovchenko et al., Phys. Rev. C **94** (2016) 024906.

[2] I. Karpenko, P. Huovinen, and M. Bleicher, Comput. Phys. Commun. **185** (2014) 3016.

[3] D. Lohner [ALICE Collaboration], J. Phys. Conf. Ser. **446** (2013) 012028.

DOI:10.15120/GR-2017-1

Equations of state for real gases on the nuclear scale

V. Vovchenko[1,2,3]
[1]ITP, Goethe University, Frankfurt am Main, Germany; [2]FIAS, Frankfurt am Main, Germany; [3]Taras Shevchenko University, Kiev, Ukraine

Classical models of equation of state for real gases are generalized to include quantum statistical effects [1]. The free energy of the system reads

$$F(T,V,N) = F^{\rm id}(T,V f(\eta),N) + N\,u(n), \qquad (1)$$

where $F^{\rm id}(T,V,N)$ is the free energy of the corresponding quantum ideal gas. Function $f(n)$ quantifies the fraction of the total volume which is available for particles to move in at the given value of the packing fraction $\eta \equiv bn/4$, where b is the eigenvolume parameter. The function $f(\eta)$ has to take values in the range $0 \leq f(\eta) \leq 1$, and it corresponds to a generalized excluded-volume (EV) procedure. The quantity $u(n)$ in Eq. (1) is the self-consistent density-dependent mean field, corresponding to intermediate-range attractive interactions. All other quantities are calculated from free energy via standard thermodynamic identities (see [1] for details).

A family of two-parameter models, consistent with van der Waals (VDW) equation in low-density limit, is considered. Variations on the EV mechanism include van der Waals (VDW) and Carnahan-Starling models, while the considered attractive mean fields are based on VDW, Redlich-Kwong-Soave (RKS), Peng-Robinson (PR), and Clausius equations of state, giving a total of eight different VDW-like models. All considered models are consistent with the VDW equation of state in the low-density limit and, augmented with quantum statistical effects, give a fair description of properties of symmetric nuclear matter.

The VDW parameters a and b of nucleon-nucleon interaction are fitted in each model to the properties of ground state of nuclear matter, and the following range of parameters is obtained: $a = 330 - 430$ MeV fm^3 and $b = 2.5 - 4.4$ fm^3. Fits within standard VDW model are found to underestimate the value of the attraction parameter a. In the context of excluded-volume approach, the fits to the nuclear ground state disfavor values of the effective hard-core radius of nucleon significantly smaller than 0.5 fm in the nuclear matter region of phase diagram.

All considered models provide qualitatively similar description of nuclear matter, in particular regarding the critical parameters and critical fluctuations. Differences between models are more pronounced if one compares stiffness between the resulting equations of state. This is illustrated by the density dependence of the binding energy per nucleon E/A at $T = 0$ shown in Fig. 1: The behavior of E/A is changes significantly between different real gas models at densities above the saturation density n_0. The VDW model yields the stiffest equation of state, with the nuclear "incompressibility" factor $K_0 = 9\,(\partial P/\partial n)_T \cong 763$ MeV at the saturation density. This is well above the empirical range $250 - 315$ MeV [2]. On the other hand, the model with Carnahan-Starling EV term and Clausius attraction term yields $K_0 \cong 333$ MeV, much closer to empirical estimates, and better than the $K_0 \cong 550$ MeV value obtained in the standard Walecka model [3].

The present approach allows a straightforward generalization to a multi-component hadron gas. This, in turn, opens new applications in physics of heavy-ion collisions and QCD equation of state. As an illustration, the generalization to include the baryon-baryon interactions in the full hadron resonance gas model is performed. The preliminary calculations show that the behavior of the baryon-related lattice QCD observables at zero chemical potential is strongly correlated to the nuclear matter properties.

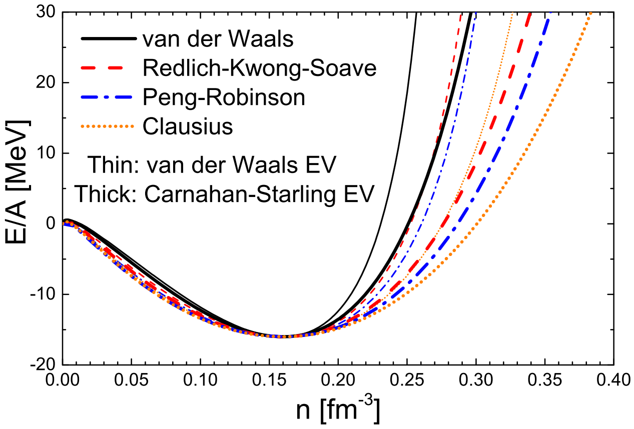

Figure 1: The nucleon number density dependence of the binding energy per nucleon E/A in symmetric nuclear matter calculated within eight different real gas models at $T = 0$. The thin lines denote calculations within four models with the VDW EV term, i.e. they correspond to VDW (solid black line), Redlich-Kwong-Soave (dashed red line), Peng-Robinson (dash-dotted blue line), and Clausius (dotted orange line) models. The thick lines correspond to models with the Carnahan-Starling EV term.

References

[1] V. Vovchenko, arXiv:1701.06524 [nucl-th].

[2] J. R. Stone, N. J. Stone, and S. A. Moszkowski, Phys. Rev. C **89** (2014) 044316.

[3] M. Dutra *et al.*, Phys. Rev. C **90** (2014) 055203.

DOI:10.15120/GR-2017-1

Shear viscosity of a pion gas[*]

J.B. Rose[1,2], *D. Oliinychenko*[1,3], *J.M. Torres-Rincon*[2], *and H. Petersen*[1,2,4]
[1]Frankfurt Institute for Advanced Studies, Frankfurt, Germany; [2]Institute for Theoretical physics, Goethe University, Frankfurt, Germany; [3]Bogolyubov Institute for Theoretical Physics, Kiev, Ukraine; [4]GSI, Darmstadt, Germany

Shear viscosity is an important transport property of strongly interacting matter. While it was first shown to play a significant role in explaining the high levels of elliptic flow observed at RHIC or the LHC in an hydrodynamical framework, there has been far fewer such investigations at lower temperatures such as will be explored at FAIR. In particular on the hadron gas side of the phase transition, these show conflicting results [1-3]. The ultimate goal of this work is to extract the shear viscosity over entropy ratio as a function of temperature and net baryon chemical potential in a full hadron gas. Here, the formalism is introduced and validity checks for a pion gas are displayed.

The viscosity calculation is based on the Green-Kubo formalism. This formalism relates so-called auto-correlation functions with themselves at a later point in time to extract transport coefficients. Viscosity can thus be expressed as

$$\eta = \frac{V}{T}\int_0^\infty C^{xy}(t)dt, \tag{1}$$

where V is the volume and T is the temperature of the system. $C^{xy}(t)$, the auto-correlation function, is computed as a discrete average over N fixed time steps:

$$C^{xy}(t) = \frac{1}{N}\sum_s^N T^{xy}(s)T^{xy}(s+t), \tag{2}$$

with T^{xy} an off-diagonal spatial component of the energy-momentum tensor.

The model used in all calculations is SMASH [4], a new transport approach. Since a constant temperature over a long period of time is required by the previously described formalism, all calculations are performed in a box with periodic boundary conditions simulating infinite matter.

As a test on the calculation, we reproduce analytical calculations for a gas of pions with constant isotropic cross-sections (figure 1). All plots show the computed shear viscosity from SMASH and compare it to calculations within a high order Chapman-Enskog approximation [5]. The three plots in the left column show the viscosity as a function of the physical parameters which come into play in the analytical calculations, namely the temperature, cross-section and mass of the pions, and agree with analytical calculations up to a difference of no more than 3%. The three plots on the right show that the calculation is very stable against large variations of other technical parameters. Specifically, these are the number of box calculations (which does not strongly affect results if one uses more than a thousand), the density ratio (the ratio of the current density to the thermal density for $\mu = 0$, for which a very slow dependence is shown, with a maximum error of about 6%) and the number of used test particles (which remains relatively stable within 4% of the Chapman-Enskog value).

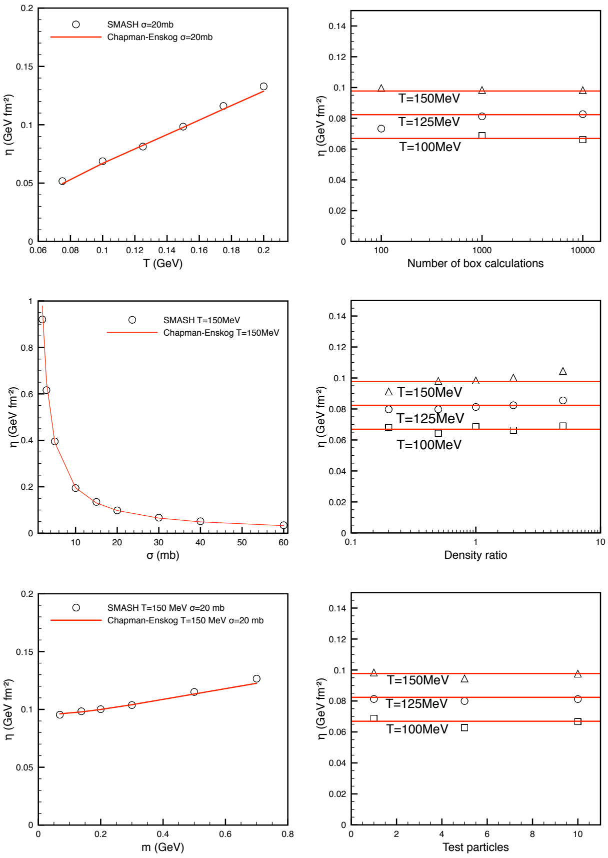

Figure 1: Pion box systematics.

Following this detailed verification of the method, the calculation of the shear viscosity of the complete hadron gas is ongoing.

References

[1] N. Demir, S. Bass, Phys.Rev.Lett. 102 (2009) 172302
[2] H. Song, S. Bass, U. Heinz, Phys.Rev. C83 (2011) 024912
[3] P. Romatschke, S. Pratt, arXiv:1409.0010 [nucl-th]
[4] J. Weil et al., Phys. Rev. C94 (2016) no.5, 054905
[5] J. Torres-Rincon, PhD dissertation (2012)

---

[*] Work supported by HIC4FAIR/HGS-Hire/Helmholtz Young Investigator Group VH-NG822

Spectral functions of the quark-meson model within the functional renormalization group approach beyond the local potential approximation*

A. Stegemann†[1], *R.-A. Tripolt*[3], *L. von Smekal*[2], *and D.-H. Rischke*[1]

[1]Johann Wolfgang Goethe-Universität Frankfurt am Main; [2]Justus-Liebig-Universität Gießen; [3]European Centre for Theoretical Studies in Nuclear Physics and Related Areas (ECT*) Trento

Introduction

In order to study the low-energy regime of quantum chromodynamics (QCD), where quarks and gluons are confined into hadrons, it is necessary to employ non-perturbative methods. In this work, we use the functional renormalization group (FRG) which, in contrast to lattice calculations, does not exhibit a sign problem at finite quark-chemical potential. We apply this method to the quark-meson-model, an effective theory for low-energy QCD that incorporates quarks (ψ) as well as scalar (σ) and pseudoscalar (π) mesonic degrees of freedom.

Functional renormalization group

The FRG approach aims at calculating the effective action Γ which is the generating functional of the one-particle irreducible diagrams in the considered theory. Therefore, the scale (k)-dependent effective average action Γ_k is introduced. It interpolates between the classical action S in the ultraviolet and the full effective action in the infrared. This behavior is described by the FRG flow equation, also known as Wetterich equation [1].

The Wetterich equation is a functional differential equation. In order to solve it, one needs to expand the effective average action and truncate this expansion which yields a finite set of coupled differential equations. One possibility is the derivative expansion which corresponds to an expansion in momenta and reads for a scalar field ϕ [2]

$$\Gamma_k = \int \mathrm{d}^D x \left[U_k\left(\phi^2\right) + \frac{1}{2} Z_k\left(\phi^2\right)\left(\partial_\mu \phi\right)^2 + \mathcal{O}\left(\partial^4\right)\right].$$

In the lowest order derivative expansion, usually called local potential approximation (LPA), the only scale-dependent quantity is the effective potential U_k. The next order, denoted as LPA$'$, additionally incorporates a scale- (but not yet field-)dependent wave function renormalization Z_k.

Spectral functions from the FRG

When performing calculations in quantum field theory at finite temperature, it is convenient to work in Euclidean space-time. However, this causes the need for an analytic continuation when trying to calculate real-time quantities like spectral functions.

Within the FRG framework, such an analytic continuation procedure is possible already on the level of the flow equations. This method has been applied to the 2-flavor quark-meson-model in previous studies [3,4].

However, these calculations, which were restricted to the LPA, show a large difference between the pion pole and curvature masses at vanishing quark-chemical potential and small temperature. It is presumed that the use of higher truncations can solve this problem. Evidence was found that the LPA$'$ can already be sufficient [5].

Extension to LPA$'$

In our recent calculations, we included mesonic wave function renormalizations $Z_{\sigma,k}$ and $Z_{\pi,k}$. At finite temperature, they split up into a longitudinal and transversal part with respect to the heat bath. Thus, our ansatz contains five scale-dependent quantities.

We derived the flow equations for the effective potential as well as for the wave function renormalizations and for the spectral functions. Currently, we are occupied with the numerical solution; first results look promising.

In the near future, we will complete the numerical solution of the flow equations. Later, we plan to include additionally a fermionic wave function renormalization $Z_{\psi,k}$ and a scale-dependent Yukawa coupling.

References

[1] C. Wetterich, “Exact evolution equation for the effective potential”, Phys. Lett. B 301, 90 (1993).

[2] H. Gies, “Introduction to the functional RG and applications to gauge theories”, Lect. Notes Phys. 852, 287 (2012).

[3] R.-A. Tripolt, N. Strodthoff, L. von Smekal, and J. Wambach, “Spectral Functions for the Quark-Meson Model Phase Diagram from the Functional Renormalization Group”, Phys.Rev. D89, 034010 (2014).

[4] R.-A. Tripolt, L. von Smekal, and J. Wambach, “Flow equations for spectral functions at finite external momenta”, Phys.Rev. D90, 074031 (2014).

[5] A. J. Helmboldt, J. M. Pawlowski, N. Strodthoff, “Towards quantitative precision in the chiral crossover: masses and fluctuation scales”, Phys.Rev. D91, 054010 (2015).

---

* A. S. thanks GSI F&E and HIC for FAIR for funding.

† stegemann@th.physik.uni-frankfurt.de

DOI:10.15120/GR-2017-1

Scaling violation and the magnetic equation of state in chiral models[*]

G. A. Almasi[†1], *B. Friman*[1,2], *K. Redlich*[2,3,4], *and W. Tarnowski*[5]

[1]Gesellschaft für Schwerionenforschung, GSI, D-64291 Darmstadt, Germany; [2]ExtreMe Matter Institute (EMMI), D-64291 Darmstadt, Germany; [3]University of Wrocław - Faculty of Physics and Astronomy, PL-50-204 Wrocław, Poland; [4]Department of Physics, Duke University, Durham, NC 27708, USA; [5]Faculty of Physics, Astronomy and Applied Informatics, Jagiellonian University, PL-30-348 Cracow, Poland

In this work, the scaling behavior of the order parameter at the chiral phase transition, the so-called magnetic equation of state, of strongly interacting matter is studied within effective models. We explore universal and nonuniversal structures near the critical point. We consider two models in the mean-field approximation, the quark-meson (QM) and the Polyakov loop extended quark-meson (PQM) models, and compare their critical properties with a purely bosonic theory, the $O(N)$ linear sigma (LS) model in the $N \to \infty$ limit. In these models the order parameter scaling function is found analytically using the high temperature expansion of the thermodynamic potential. The effects of a gluonic background on the nonuniversal scaling parameters are studied within the PQM model.

Fig. 1 shows that in the quark-meson model the scaling violation is small up to physical pion mass, in agreement with recent lattice calculations [2]. The coupling of quarks to the Polyakov loop enhances the scaling violation, as seen in Fig. 2. This is particularly apparent in the broken phase.

The difference in strength of the scaling violation found in the QM and PQM models is even more pronounced in the $O(N)$ sigma model. As shown in Fig. 3, the $O(N)$ model exhibits stronger deviations from the universal scaling curve for the corresponding strength of the symmetry breaking field and scaling is preserved only for a very weak external field. The qualitative differences in the universal scaling curves and in the strength of the scaling violation indicate that fluctuations of the meson fields, not accounted for in the mean-field models, play an important rôle. The strong violation of scaling obtained in this model is consistent with previous studies within the FRG approach [3].

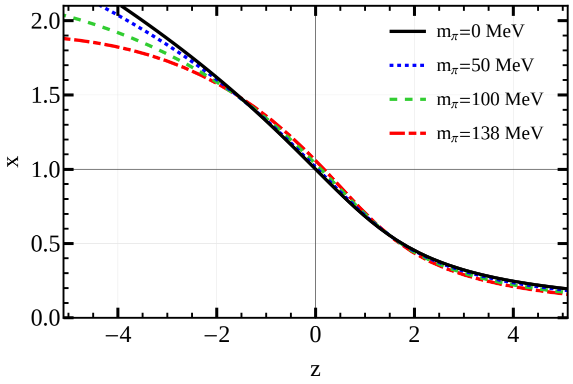

Figure 1: The magnetic equation of state for the QM model. The black line corresponds to the universal scaling curve.

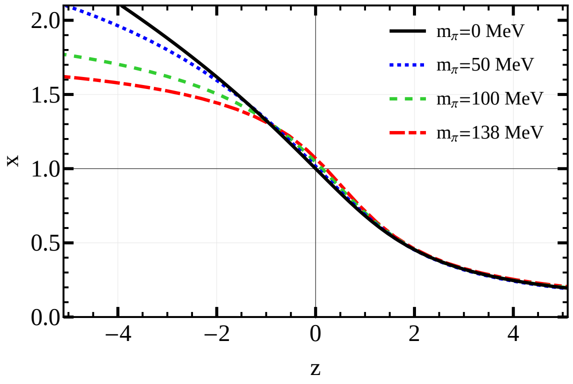

Figure 2: The magnetic equation of state for the PQM model.

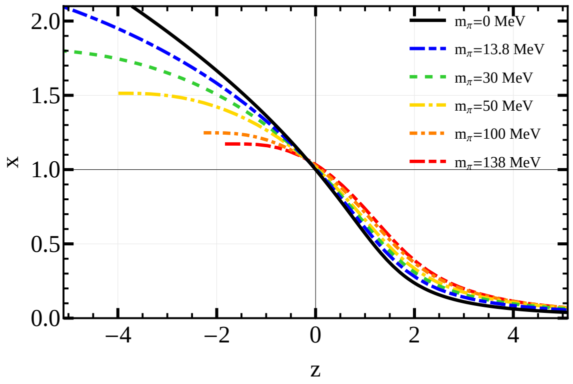

Figure 3: The magnetic equation of state for the $O(N)$ linear sigma model in the $N \to \infty$ limit.

References

[1] G. A. Almasi, B. Friman, K. Redlich and W. Tarnowski, Phys. Rev. D **95**, 014007 (2017).

[2] H.-T. Ding and P. Hegde. 2015. (Bielefeld-BNL-CCNU), Proc. Sci. LATTICE, 161 (2016).

[3] J. Braun, B. Klein and P. Piasecki, Eur.Phys.J. C **71**, 1576 (2011).

---

[*] The work of B.F. and K.R. was partly supported by the Extreme Matter Institute EMMI. K. R. also acknowledges partial supports of the Polish Science Center (NCN) under Maestro Grant No. DEC-2013/10/A/ST2/00106, and the U.S. Department of Energy under Grant No. DE-FG02-05ER41367. W.T. is grateful to GSI for the hospitality during the Summer Student Programme. G. A. acknowledges the support of the Hessian LOEWE initiative through the Helmholtz International Center for FAIR (HIC for FAIR).

[†] g.almasi@gsi.de

DOI:10.15120/GR-2017-1

Coherent hypernucleus production in $\bar{p}A$ interactions as a test of κ meson exchange[*]

A.B. Larionov[1,2] *and H. Lenske*[1]

[1]Institut für Theoretische Physik, Universität Giessen, D-35392 Giessen, Germany; [2]National Research Center ”Kurchatov Institute”, 123182 Moscow, Russia

Coherent annihilation of antiprotons on nuclei to hyperonic channels is an efficient mechanism of populating discrete states of hypernuclei. We have studied the

$$\bar{p} + {}^{A}Z \to {}^{A}_{\Lambda}(Z-1) + \bar{\Lambda} \qquad (1)$$

annihilation reaction on a target nucleus ${}^{A}Z$ leading to the production of the hypernucleus ${}^{A}_{\Lambda}(Z-1)$. The amplitude of the $\bar{p}p \to \bar{\Lambda}\Lambda$ reaction was evaluated by considering t-channel exchange of the light strangeness-carrying mesons, i.e. pseudoscalar K, vector K^*, and the hypothetical scalar $\kappa/K_0^*(800)$, modelling correlated πK exchange in the 0^+ $I = 1/2$ channel. The parameters of the elementary $\bar{p}p \to \bar{\Lambda}\Lambda$ amplitude, i.e. vertex coupling constants, form factor cutoffs and the attenuation factor due to initial/final state interaction (ISI/FSI), were adjusted to describe the $\bar{p}p \to \bar{\Lambda}\Lambda$ cross section for beam momenta $p_{\rm lab} \simeq 1.5-8$ GeV/c. In this way we have defined two sets of parameters: without κ exchange (set 1) and with κ exchange (set 2). Both parameter sets reproduce the angle-integrated $\bar{p}p \to \bar{\Lambda}\Lambda$ cross section reasonably well. The corresponding angular distributions, however, are better described with κ exchange which significantly rises the cross section at forward scattering angles. We have evaluated the amplitude of the process Eq.(1) in second order perturbation theory by impulse approximation as discussed in detail in [1], also including antibaryon-nucleus ISI and FSI effects similar to our investigations in [2]. The wave functions of the initial nucleon and final Λ bound states were obtained numerically as stationary solutions of the corresponding Dirac equations. Self-energies were approximated by scalar and vector relativistic mean-field potentials with pre-chosen Woods-Saxon form factors. The nucleonic potential parameters were adjusted to the total binding energy of the target nucleus and the r.m.s. radii of proton and neutron HFB ground state matter densities. As in [3] the Λ single particle states were obtained by potential fits to the energy spectrum of the final hypernucleus.

Numerical calculations have been performed for the reaction $\bar{p} + {}^{40}\text{Ar} \to {}^{40}_{\Lambda}\text{Cl} + \bar{\Lambda}$. The choice of the ^{40}Ar target was motivated by the future PANDA experiment at FAIR where noble gases will be used as targets. In order to assure that after the reaction the residual ^{39}Cl core nucleus carries as little excitation energy as possible, we consider only strangeness creation processes on protons of the ^{40}Ar $1d_{3/2}$ valence shell. As we see from Fig. 1, the cross section of coherent hypernucleus production grows rapidly with orbital angular momentum of the Λ state. The inclusion of κ exchange leads to almost one order of magnitude larger hypernucleus production cross sections. A closer inspection shows that the enhancement due to κ exchange is, in fact, a result of a general property of bound state Dirac wave functions. Their low energy characteristics lead to a strong suppression of the lower components which, in turn, suppresses any kind of pseudoscalar vertices involving the γ^5 matrix – which mixes upper and lower components – as encountered in the K-meson exchange. Thus, the apparent in-medium enhancement of the κ exchange amplitude is in fact related to a relative suppression of the pseudoscalar K exchange amplitude. As a consequence, the coherent hypernucleus production reactions proceed predominantly via K^* and κ exchange where the latter – when included – dominates, especially at beam momenta of interest for the PANDA experiment, irrespective of the quantum state in which the Λ hyperon is produced. Hence, we conclude that coherent hypernucleus production in $\bar{p}A$ collisions could serve as a test for κ-meson exchange in the underlying $\bar{p}p \to \bar{\Lambda}\Lambda$ transition amplitude.

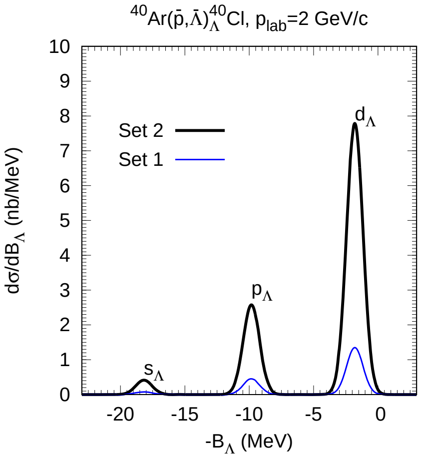

Figure 1: The Λ binding energy spectrum of the ${}^{40}_{\Lambda}$Cl hypernuclei coherently produced in $\bar{p}\,{}^{40}$Ar collisions at $p_{\rm lab} = 2$ GeV/c. The calculated spectrum was folded by Gaussians of a width $\Gamma_{FWHM} = 1.5$ MeV.

References

[1] A.B. Larionov, H. Lenske, PLB (submitted); arXiv:1703.02073.

[2] A.B. Larionov and H. Lenske, Nucl. Phys. **A957**, 450 (2017).

[3] S. Bender, R. Shyam, H. Lenske, Nucl. Phys. **A839**, 51 (2010).

---

[*] Work supported by DFG under Grant No. Le439/9.

Investigation of heavy tetraquarks by means of lattice QCD*

A. Peters[1], *K. Cichy*[1,2], *B. Wagenbach*[1], *and M. Wagner*[1]
[1]Goethe-Universität Frankfurt am Main, Institut für Theoretische Physik, Max-von-Laue-Straße 1, D-60438 Frankfurt am Main, Germany; [2]Adam Mickiewicz University, Faculty of Physics, Umultowska 85, 61-614 Poznań, Poland

Tetraquark systems are expected to be studied in more detail in the near future by experimental collaborations, e. g. with the PANDA experiment at FAIR. Therefore it is important to gain theoretical understanding of these systems. Moreover, quite a number of mesons observed experimentally (e.g. at LHCb and Belle) are theoretically not well understood yet.

In a recent study [1] we investigate static-light $\bar{b}\bar{b}ud$ four-quark states in the Born-Oppenheimer approximation. The potential of a pair of B mesons is computed using Wilson twisted mass lattice QCD with two flavours of degenerate dynamical quarks. Using the fit function $V(r) = -\frac{\alpha}{d}\exp(-(r/d)^2)$ we provide fits to the ground state potentials in the attractive channels and discuss the potentials in the repulsive and excited channels. The attractive channels are most important since they can possibly lead to a bound four-quark state, i.e. a $\bar{b}\bar{b}ud$ tetraquark. Using these attractive potentials in the Schrödinger equation, we find indication for such a tetraquark state of two static bottom antiquarks and two light u/d quarks with mass extrapolated down to the physical value (cf. Figure 1). In another study [2, 3] of the same four-quark system we investigate the dependence of the binding of the four quarks on the mass of the light quarks. While we find strong indication for a bound four-quark state for $qq = (ud-du)/\sqrt{2}$, i.e. isospin $I = 0$, which is stable with respect to QCD, i.e. can only decay weakly, we find clear evidence against the existence of corresponding tetraquarks with $qq \in \{uu, (ud+du)/\sqrt{2}, dd\}$, i.e. isospin $I = 1$, $qq = ss$ and $qq = cc$. In a follow-up study [4] we investigate heavy-light four-quark systems $\bar{b}\bar{b}ud$ with bottom quarks of finite mass which are treated in the framework of NRQCD. We focus on $I(J^P) = 0(1^+)$, where we recently found evidence for the existence of a tetraquark state using static bottom quarks.

One example for an experimentally measured but not well understood system is the $Z_c^{\pm}$. It contains a $c\bar{c}$ pair, which one can infer from both its mass and decay products. Because it carries electromagnetic charge, there must be additional quarks, most likely a light quark-antiquark pair, i.e. the minimal quark content of $Z_c^{\pm}$ is $c\bar{c}q\bar{q}$ with $q = u, d$. For this reason they are subject of many recent experimental and theoretical investigations. Such $c\bar{c}$ studies are expected to be measured by PANDA. In our study [5] we investigate as a first step the $Z_b^{\pm}$ which is quite similar to $Z_c^{\pm}$. We assume a four-quark structure $b\bar{b}u\bar{d}$ using lattice QCD. Again, we work with b quarks in the static approximation. We compute the potentials of the static quarks in the presence of the light quarks, which can be interpreted as the potentials of a B and a $\bar{B}$ meson. To check, whether the four quarks may form a bound state, we use the Born-Oppenheimer approximation, i.e. we solve the Schrödinger equation with the computed potentials. We find first evidence that $B\bar{B}$ with light quarks $qq = u\bar{d}$ and quantum numbers $I(J^P) = 1(1^+)$ is a candidate for a stable tetraquark. In the future we plan to replace the heavy b quarks by lighter c quarks.

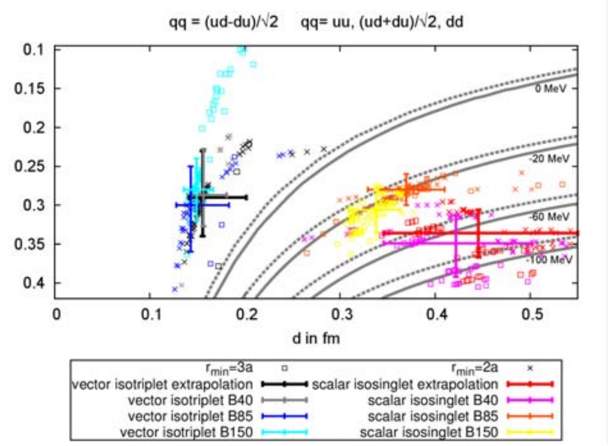

Figure 1: Binding energy isolines $E_B(\alpha, d) = \mathrm{const}$ in the $\alpha - d$ plane for the scalar isosinglet ($I = 0$, $j = 0$) and vector isotriplet ($I = 1$, $j = 1$) channels and four pion masses: 140 MeV (extrapolated), 340 MeV, 480 MeV and 650 MeV. The error bars represent combined systematic and statistical errors. The area below the 0 MeV line corresponds to a bound state, the area above corresponds to a two-meson state.

References

[1] P. Bicudo, K. Cichy, A. Peters and M. Wagner, Phys. Rev. D **93** (2016) [arXiv:1510.03441 [hep-lat]].

[2] P. Bicudo, K. Cichy, A. Peters, B. Wagenbach and M. Wagner, Phys. Rev. D **92** (2015) [arXiv:1505.00613 [hep-lat]].

[3] A. Peters, P. Bicudo, K. Cichy, B. Wagenbach and M. Wagner, PoS LATTICE **2015** (2016) 095 [arXiv:1508.00343 [hep-lat]].

[4] A. Peters, P. Bicudo, L. Leskovec, S. Meinel and M. Wagner, PoS LATTICE **2016** (2016) 104 [arXiv:1609.00181 [hep-lat]].

[5] A. Peters, P. Bicudo, K. Cichy and M. Wagner, J. Phys. Conf. Ser. **742** (2016) [arXiv:1602.07621 [hep-lat]].

---

* Work supported by HIC4FAIR/HGS-HIRe

DOI:10.15120/GR-2017-1

Improved operation for the ALICE Tier2 Centre at GSI

K. Schwarz, S. Fleischer, R. Grosso, J. Knedlik, T. Kollegger[1]
[1]GSI, Darmstadt, Germany

This article describes the improvements implemented in 2016 to increase the reliability and performance of the ALICE Tier2 Computing Centre at GSI.

ALICE Tier2 centre at GSI and ALICE Grid in Germany

The ALICE Tier2 centre and the National Analysis Facility at GSI provide a computing infrastructure for ALICE Grid and for the local usage of the German ALICE groups.

The storage resources pledged to the global ALICE community (2300 TB) are provided via a Grid Storage Element which consists of a set of xrootd daemons running on top of the Lustre file system.

The main elements are the xrootd redirector in combination with three xrootd data servers as well as two xrootd forward proxy servers, also for redundancy. The redirector of the GSI storage element is using the split directive of xrootd and redirects external clients to the external interfaces of the xrootd data server machines and internal clients to the internal interfaces which are directly connected to the local Infiniband Cluster. The xrootd forward proxy servers provide the possibility to Grid jobs running inside the protected HPC environment to read input data from external data sources using the proxy interface. Writing to external storage elements is possible via the same technique. The complete setup can be seen in fig. 1.

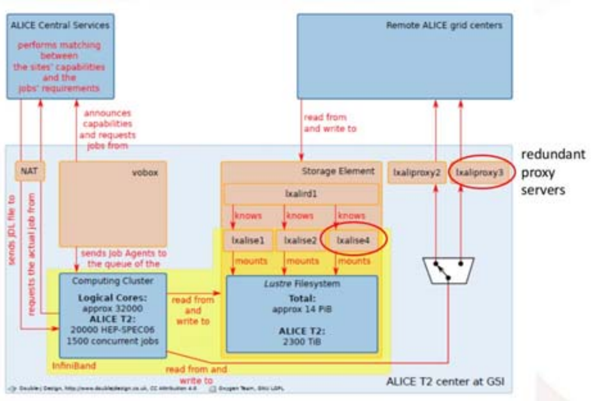

Figure 1: ALICE tier centre at GSI

Throughout the year GSI participates in centrally managed ALICE Grid productions and data analysis activities, but also analysis jobs of individual users are running on the ALICE Tier2 centre. The overall job share of successfully computed jobs in 2016 contributed by the German Grid sites, the GSI Tier2 centre and Forschungszentrum Karlsruhe (ALICE tier1 centre) has been 6.3% of all ALICE Grid jobs worldwide. This corresponds well with the pledged CPU resources for 2016: 16000 HEP-SPEC06 for GSI Tier2 (7% of the global Tier2 requirements) and 39250 HEP-SPEC06 for FZK (25% of the global T1 requirements)

Since Spring 2016 the ALICE Tier2 centre is running within GSI's Green IT Cube.

Singularity

A specific container technology - Singularity - has been adopted in the ALICE Tier2 centre at GSI in order to encapsulate ALICE jobs in an experiment specific system image. This made it possible to run ALICE Grid jobs smoothly in their standard Scientific Linux environment on top of the Debian based host system of the local HPC cluster. A detailed description of the related configuration and workflow can be found in [1].

Key Performance Indicator

High-level performance indicators, such as delivered computing wall time or Storage Element availability are being monitored and show the overall status of the ALICE Tier2 centre. Furthermore, a tool has been developed which identifies how jobs performed before and after they have been submitted to GSI. This helps putting the absolute job success rate into context and makes it easier to recognize if the GSI ALICE Tier2 centre is performing well.

XRootD Plugins

In order to optimise the current storage infrastructure, namely the access to Lustre through XRootD data servers, several XRootD Plugins have been developed. One solution provided is a client and a server based Plugin which is able to redirect XRootD file operations directly to Lustre thus bypassing the need for Grid jobs running at GSI to double the network traffic by first communicating with the XrootD data servers. A second solution provided is a Plugin which reports to the central ALICE Grid Monitoring the ALICE Grid quota on Lustre instead of the full Lustre capacity provided at GSI as it did before. The implementations are described in [2].

References

[1] R. Grosso, M. Bauer, S. Fleischer, J. Knedlik, T. Kollegger, K. Schwarz, “Use of Singularity containers for the ALICE T2”, GSI Scientific Report 2016

[2] J. Knedlik, P. Kramp, “Adapting XRootD to the site specific infrastructure at GSI”, GSI Scientific Report 2016

DOI:10.15120/GR-2017-1

Adapting XRootD to the site specific infrastructure at GSI

J. Knedlik[1] *and P. Kramp*[1]
[1]GSI, Darmstadt, Germany

Abstract

Operating an XRootD service, the established software standard for WAN data access in HEP and HENP, to access the scientific data stored on-top of the HPC infrastructure at the ALICE Tier 2 centre at GSI revealed multiple challenges and requirements. This article describes the current state of development for XRootD based solutions, especially XRootD client & server plug-ins.

ALICE Tier 2 & XRootD

GSI is operating the only German ALICE Tier 2 centre. In this context GSI provides a computing infrastructure and storage to the ALICE community. In ALICE's AliEn Grid framework data is accessed through the XRootD protocol. XRootD enables the use of this data through a scalable federated storage system. At GSI, instead of operating XRootD servers with local storage, the shared HPC Lustre filesystem is used as storage backend of the XRootD servers. In AliEn, Grid jobs requiring the same data are preferably scheduled on the same site to lower the need for traffic between sites. This means, that local data is reused many times and therefore it is essential to optimize the I/O performance.

Improving the I/O performance at GSI using XRootD plug-ins

With the current storage infrastructure at GSI, namely the access to Lustre through the XRootD data servers, the following room for improvement has been identified: The three XRootD dataservers can provide limited I/O bandwidth and all data read locally via XRootD from Lustre needs to be sent over the network twice (Lustre to XrootD server & XrootD server to client), effectively doubling the network traffic for an I/O operation.

We considered two kinds of plug-ins in order to improve I/O performance, namely a client plug-in and a server plug-in. The XRootD client plug-in API offers a way to overwrite XRootD file operations. Being configurable via a local configuration file, the plug-in replaces specified remote URLs with local file paths. The current plug-in, in contrary to the version specified in last year's report[1, p. 280], uses XRootD file operations. A requirement for this version is a modified XRootD client source[2], which has been developed in cooperation with the XRootD development team and shall be integrated into the main base soon. It introduces a new component for handling local file operations, which is also necessary for a redirection to the local file system by using a server or client side plug-in. The server plug-in has the same purpose as the client plug-in. A redirector server may load this plug-in, to redirect clients to locally available files, if both client and redirection target are inside a private network, as this guarantees local availability of the required file at GSI. In order to allow a redirector to redirect to a local file, additional changes needed to be implemented into the XRootD base code. Therefore notification of the XRootD client component responsible for file operations, about accessing the file locally instead of remotely, had to be added. We also modified XRootD's communication message handling interface in order to enable the aforementioned notification. The remaining operations are handled in the same way as in the client plug-in.

Lustre quota as XRootD file space statistics using an XRootD plug-in

One of ALICE's monitoring tools reported wrong space usage statistics to CERN. It uses the onboard XRootD executable xrdfs in order to get space usage statistics from local storage elements. Since XRootD runs on top of the local Lustre filesystem, the XRootD data server returned statistics referring to the whole Lustre file space instead of ALICE's Grid quota at GSI. This in turn gave misleading information to ALICE's distributed data management system. Our deployed solution was to use the XRootD - data server - plug-in API to create a plug-in that feeds Lustre quota statistics collected by using the Lustre C-API to our data servers instead of using the base XRootD calls.[3]

Conclusion

In conclusion we have implemented XRootD plug-ins redirecting client I/O to data on Lustre which has the capability to significantly improve the I/O performance. We proposed implementation changes in the core XRootD code to allow robust usage of such plug-ins. A data server plug-in for Lustre quota statistics has been deployed. The current tests give promising results and show that plug-ins can be used to adapt XRootD to our site's specific needs.

References

[1] "GSI Scientific Report 2015", doi = 10.15120/GR-2016-1, http://dx.doi.org/10.15120/GR-2016-1

[2] https://github.com/pkramp/xrootd/tree/local-file-impl_localfilehandler

[3] https://github.com/jknedlik/XrdLustreOssWrapper

Use of *Singularity* containers for the ALICE Tier2 at GSI

R. Grosso[1], *M. Bauer*[1], *S. Fleischer*[1], *J. Knedlik*[1], *T. Kollegger*[1], *and K. Schwarz*[1]
[1]GSI, Darmstadt, Germany

A specific container technology - *Singularity* - has been adopted in the GSI ALICE Tier2 site to encapsulate ALICE jobs in an experiment-specific system image, thus allowing to run in the locally shared HPC environment. The use of *Singularity* in this context and the resulting benefits are presented.

Container technologies and Singularity

As an ALICE Tier2 site, GSI provides storage and computational resources integrated in the Grid of the experiment via its middleware, *AliEn*. This assumes a standard environment, notably a specific operating system. Appropriately chosen container technologies can help considerably to fit these requirements into a shared cluster.

Containers are a thin layer encapsulating a system environment, from a user perspective looking like lightweight virtual machines. The user can install his own software in a container, without affecting other containers or the host environment, on which the container runs. Since containers include neither hardware virtualization nor a kernel, their footprint is significantly smaller than that of a virtual machine and applications in a container run at the same level as native applications.

Containers have become very popular in the last years as an enterprise solution for running many isolated instances of a definite working environment on a single machine. They could in addition effectively satisfy a strong demand in the science domain too, offering a way to insure application and environment compatibility. The most popular container system, *Docker*[1], which is at the origin of the dissemination of container technology of the last years, has not yet matched this request in HPC environments, mostly due to security issues. A relatively new container framework - *Singularity*[2][3] - overcomes these problems. The strongest point for the adoption of *Singularity* as a container solution on a shared HPC cluster is **security**. The user inside a *Singularity* container is the same as the user on the host. Privilege escalation within the container is not possible and there is no root-owned container daemon, which are all important points in favor of this technology both in terms of security and of effective resource management. In addition the image is provided as a single file, which makes it very portable.

Implementation at the GSI ALICE Tier2 site

Prerequisite for running jobs within a *Singularity* image is the installation of *Singularity* on the cluster. The node requesting the resource manager to launch jobs on behalf of ALICE (VOBox) must prepend the script call with the `singularity` command and its flags. This is implemented in a wrapper command taking precedence over the default command for launching batch scripts (`sbatch`).

On a building host a definition file describes the system image, specifying for example the list of packages which have to be installed, and is used by `singularity bootstrap` to make the image. By adapting the definition file to ALICE-specific requirements, we can provide within the *Singularity* image expected packages and the expected environment (e.g. we had to correct the definition of locales via environment variables). Correspondingly adapting the system and the environment on a dedicated cluster would have required considerably more work, but would not even have been possible on a shared HPC cluster, as is our case.

AliEn jobs running in the container need to read also from a CernVM File System mounted on the cluster. That is possible by means of the `--bind` option, with which the specified destination is bind mounted in the container. AliEn jobs also need to write output to a specified location, within the `/tmp` directory. These did not require any additional setting, as *Singularity* automatically shares `/tmp` into the container. However we needed to set the user home directory in the container to a valid path. That is achieved by means of the `--homedir` flag, requiring only that the directory exists in the container to serve as a mount point. This is just one additional line in the definition's file. To keep synchronized with the experiments standard running environment, the definition file has to be updated when needed, and the image must be regenerated and newly deployed on the CernVM File System, where it is seen by jobs from all worker nodes. In case, the `singularity` command line in the sbatch wrapper on the VOBox machine is also updated.

This workflow has allowed to operate the ALICE Tier 2 site at GSI, transparently running AliEn jobs in their standard Scientific Linux 6 environment on top of the Debian host system of the local HPC cluster and substantially reducing possible causes for failing jobs together with the load of debugging and fixing them.

References

[1] https://www.docker.com

[2] G. M. Kurtzer, “Singularity 2.1.2 - Linux application and environment containers for science”, August 2016, doi = 10.5281/zenodo.60736, https://doi.org/10.5281/zenodo.60736

[3] http://singularity.lbl.gov

DOI:10.15120/GR-2017-1

Machine learning based monitoring of HEP computing infrastructures[*]

A. Gomez Ramirez[1], *C. Lara*[1], *and U. Kebschull*[1]
[1]Infrastructure and Computer Systems for Data Processing (IRI), Goethe-University Frankfurt

Introduction

Computing infrastructures used in High Energy Physics (HEP) need tools to monitor, analyze and react to potential security incidents. These tools should collect data such as resource consumption, system logfiles and sequence of system calls for detecting and analyzing anomalies caused by security problems. They should also be able to perform automated actions when an attack is detected without the administrator intervention. We are working in a framework that accomplishes these requirements, with a proof of concept implementation for the AliEn Grid used by the LHC experiment ALICE, also used in the Grid site at GSI. We show how we achieve a fully virtualized environment that improves the security by isolating services and jobs. We describe a collected dataset for Machine Learning based Intrusion Prevention and Detection Systems. This dataset is composed of resource consumption (such as CPU, RAM and network traffic), system logfiles, and system call data collected from production jobs running in a Grid test site and a big set of malware. This malware was collected from security research sites. Based on this dataset, we will proceed to develop Machine Learning algorithms able to detect malicious jobs.

Implementation

We have deployed a Grid site based on AliEn [1] in a local Linux cluster, with 5 Ubuntu 14.04 nodes. To orchestrate and run the jobs inside Linux Containers (LC) we have tested 3 different tools: Google Kubernetes, Apache Mesos and Docker Swarm.

We have decided to work with Docker Swarm, given its more simplistic setup. As LC engine we use Docker with Centos 6 container images. We have developed AliEn interfaces for the mentioned resource management system. CVMFS [2] is installed at the hosts and shared as a volume inside the AliEn container, to allow access to HEP libraries. Currently we execute one Job per container. This is useful to increase the traceability between different jobs. Also, this is the natural micro service model for LC.

We have used Prometheus [3] and Sysdig [4] as the monitoring infrastructure for collecting data from normal Grid jobs. Prometheus allows to take resource usage data directly from containers and collect it by a RESTful interface. Sysdig enables system call capture in Linux OS, in a fast and reliable way. We have developed a custom Python library to integrate these tools, and make them fit our needs. This infrastructure has been utilized for the execution and measurement of AliEn production jobs, that are tagged as normal jobs.

A network isolated machine for malware data collection was used, with the same setup as the Grid worker nodes. We have downloaded a set of 10000 Linux malware samples from a security research web site [5]. We ran the samples and collected the same information as for the normal jobs (logfiles, sequence of system calls, resource usage data). At the end we obtained a dataset that allows to train and test our selected Machine Learning algorithms: SVM, Radial Basis Function NN and Deep Learning NN. Figure 1 shows a representation of the proposed framework.

Next steps

Using the described dataset, we will proceed to test the selected Machine Learning algorithms to find the one that offers the best accuracy and performance.

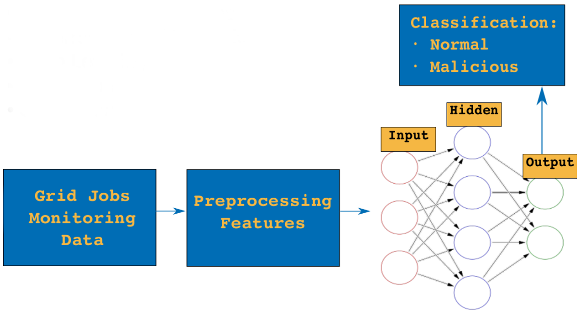

Figure 1: Data obtained from the monitored Grid jobs is processed to extract feature that feed a ML algorithm. This algorithm decides whether a job is normal or malicious.

References

[1] A. Gomez Ramirez, C. Lara and U. Kebschull, “Intrusion Prevention and Detection in Grid Computing - The ALICE Case“. JPCS 2015

[2] P Buncic et al., “CernVM - a virtual appliance for LHC applications“. Proceedings of the XII. International Workshop on Advanced Computing and Analysis Techniques in Physics Research (ACAT08), Erice, 2008 PoS(ACAT08)012

[3] https://prometheus.io/

[4] http://www.sysdig.org/

[5] https://virusshare.com/

---

[*] Work supported by HGS-HIRe, BMBF and the ALICE offline group.

FairMQ status

A. Rybalchenko[1] *and M. Al-Turany*[1]
[1]GSI, Darmstadt, Germany

The FairRoot framework provides a set of tools for simulation, reconstruction and data analysis for particle physics experiments [1]. A message queue aware package (FairMQ) has been introduced to FairRoot that enables reconstruction and analysis of free streaming data [2] [3]. Moreover it makes it possible for user code to run in a distributed and heterogeneous environment with minimum effort from the user. FairMQ devices are independent processes that can be coordinated and synchronized (if necessary) by an external mechanism through the internal state machine of the device. Furthermore, processes using FairMQ can be configured via extensible configuration system. The communication layer in FairMQ has an abstract interface that hides the transport implementation from the user code, which allows changing the transport layer without changing the user code. In addition to two existing transport implementations (with ZeroMQ [4] and nanomsg [5]) a new one, using shared memory, has been introduced. Following is a brief description of this and other FairMQ developments:

Shared memory transport

A new implementation of the transport interface using shared memory has been introduced. The shared memory transport becomes relevant when devices on the same node want to transport/share large messages. The implementation avoids copying of the message body, which can significantly improve performance and reduce CPU usage with large messages. The implementation uses Boost.Interprocess [6] library for the management of the shared memory and ZeroMQ [4] library for the transfer of the meta data associated with every message. Fig. 1 shows the transfer rate between two processes on the same node using the shared memory transport implementation. In addition to high performance, the shared memory transport also has much lower CPU usage compared to existing TCP/IPC transports.

Multiple transports per device

Introduction of the shared memory transport provided an important use case for combining more than one transport implementation within the same device: a device might want to receive data over network and send it further via shared memory. To support this use case FairMQ now allows to configure the transport on a per-channel basis.

Figure 1: Shared memory transport transfer rate

Callback-based API

A new set of APIs has been introduced to FairMQ with the goal to simplifiy implementation of common device use cases. These APIs allow the device developers to provide callbacks to device channels, that will be called whenever data arrives on the corresponding channel. FairMQ manages the callback with respect of the state machine, ensuring they are called only during allowed states.

Boilerplate reduction

To further simplify the work of device developers FairMQ now supplies a common header file that provides a main() function that handles the necessary setup and control of the device. The device developer only needs to include this file and implement two functions - one returning the device class to use and another to extend the command line options (if necessary).

References

[1] M. Al-Turany et al.: The FairRoot framework, Journal of Physics: Conference Series (2012)

[2] M. Al-Turany, A. Rybalchenko: GSI Scientific Report: Streaming data processing with FairMQ (2013)

[3] M. Al-Turany, D. Klein, A. Manafov, A. Rybalchenko, F. Uhlig: Extending the FairRoot framework to allow for simulation and reconstruction of free streaming data. Accepted for publication by Journal of Physics: Conference Series (2013).

[4] ZeroMQ: http://zeromq.org/.

[5] nanomsg: http://nanomsg.org/.

[6] Boost.Interprocess: http://www.boost.org/doc/libs/1_63_0/doc/html/interprocess/.

DOI:10.15120/GR-2017-1

Message based reconstruction example in FairRoot

R. Karabowicz[1], *M. Al-Turany*[1], *D. Klein*[1], *T. Kollegger*[1], *D. Kresan*[1], *A. Lebedev*[1], *A. Manafov*[1], *A. Rybalchenko*[1], *F. Uhlig*[1], *and N. Winckler*[1]

[1]GSI, Darmstadt, Germany

Introduction

The big scale data analysis in the FairRoot will be based on the message queue transport ([1] [2]), which provides asynchronous exchange of data packets between running processes, be it on one or multiple computing nodes. The communication between processes is realized by a transport layer, FairMQ, which currently builds on ZeroMQ or nanomsg transport.

The performance achieved for the previously implemented examples [3] encouraged the introduction of a new example that shows the transition from the single process data analysis (default in FairRoot) to multiprocess reconstruction.

FairMQ devices

The base component of FairMQ is a device. The device encapsulates tasks, provides simple functionalites and runs as a single process. The FairMQ framework offers set of general devices, that may be used to peform basic services, like splitting or merging of the data streams, enabling access to the reconstruction parameters (parameter server).

As a part of the presented example (FairRoot/examples/MQ/9-PixelDetector) several devices have been implemented:

- FairMQEx9Sampler - reads the root file (standard output FairRoot file with data organized in branches of a ROOT tree), packs the data from requested branches into TMessage, and sends the created message to a transport layer;
- FairMQEx9TaskProcessor - templated class, which unpacks data from the received message, runs the attached FairRoot task to process the data, packs the reconstructed data into messages, and finally moves the created message into transport layer; it also gives possibility to connect to the parameter server to access the reconstruction parameters needed by tasks;
- FairMEx9Sink - unpacks data from the received message to store it in the output ROOT file, which mimics the output of a standard single-process FairRoot program.

These devices are able to read and write any FairRoot file, as requested by the user. The processor device is compatible with the FairRoot tasks, provided that they implement three FairMQ-specific functions: GetParList(), InitMQ() and ExecMQ(). This functionality is enabled by using the ROOT's TMessage container class, however it comes with throughput penalty, and thus increases execution time.

The step to enhance performance is to transport data without unnecessary oherheads. In the presented example a set of three similar devices shows the implementation of data transport using simple stl vectors of binary data. This shortens execution time twofold, but comes at a price of reduced generalization. In order to read or send different types of data, appropriate devices would have to be written.

Topology

The list of the FairMQ devices that run as a group together with the intended communication channels between them is called a topology. The user specifies the devices and their properties (file names, branch names, task types, etc.) in a shell script, while the attributes of communication channels (like IP and port addresses, communication type: push-pull, publish-subscribe, request-reply) are set via JSON configuration file. The schematic plot depicting simple topology is presented in Figure 1.

Figure 1: Simple topology example.

In the example, several topologies have been prepared to ilustrate various development strategies, like adding more analysis levels (first set of processors run hit finding, tracks are reconstructed on the second level and fitted on third). The user may run the devices in the interactive mode, when all devices start in separate windows, and may be steered with key combination or in the static mode, when the devices run as subprocesses in the background and need some level of automatization to at least be able to stop themselves on completion.

References

[1] A.Rybalchenko, and M.Al-Turany, "Streaming data processing with FairMQ", GSI Scientific Report 2013

[2] M. Al-Turany et al., "ALFA: A new Framework for ALICE and FAIR experiments", GSI Scientific Report 2013

[3] N. Winckler et al., "FairMQ application example in CbmRoot", GSI Scientifi Report 2014

Status of the R3BRoot framework

D. Kresan[*1], *R. Plag*[1], *B. Löher*[1, 2], *M. Heil*[1], *V. Wagner*[2], *the R^3B collaboration*[1], *and the FairRoot group*[1]

[1]GSI, Darmstadt, Germany; [2]Institut für Kernphysik, TU Darmstadt, Germany

Reactions with Relativistic Radioactive Beams (R^3B) [1] is one of the future experiments at the FAIR facility. It will focus on studies of nuclear dynamics and astrophysics by performing reactions in inverse kinematics. The setup for detection of heavy fragments, protons, neutrons and gammas will be placed downstream the high-energy branch of the Super-FRS. The data coming from 10 complex detectors will be collected by a dedicated DAQ system and sent further to multiple client-side nodes running the analysis software R3BRoot. The R3BRoot framework [2] was designed to perform the calibration of the detectors and reconstruction of the reactions kinematics, completed by the high-level physics analysis. It also provides the functionality to calculate the interaction of particles with the pre-defined volumes of the R^3B setup and to simulate the response of the detectors. This is important during both stages: planning and design of the experiment as well as evaluation and understanding of the measured data.
The R^3B software is based on FairRoot [3] - a common software framework for FAIR experiments, developed at GSI. Figure 1 shows the schematic structure of R3BRoot, which functionality is delivered by the FairRoot framework and the UCESB software package.

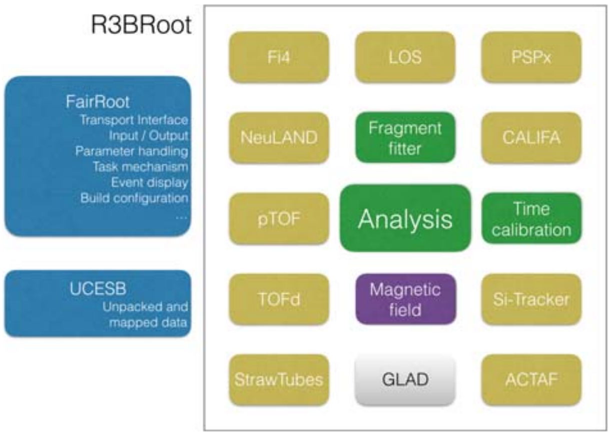

Figure 1: Basic components of the R^3B software. Yellow blocks for detectors include the code for calibration, reconstruction, and analysis. The analysis block is the combined high-level physics analysis. Green boxes are the additional algorithms.

R3BRoot is distributed under open-source license using GitHub and currently has 12 active contributors. The C++ code contains 38510 lines of code, 38% of which are automatically tested on a nightly basis. There is a dedicated forum for the user support and a website [2] with regularly updated instructions, selected documentation, and how-tos. In July 2015 and March 2017 two ”R3BRoot Development Workshops” with approximately 30 participants each were held at GSI, focused on practical exercises in software writing and aiming at education of students.

Analysis of experimental data

The setup during the last test experiment in June 2016 at GSI SIS18 contained the start counter LOS, the tracking strip detectors PSPx, the fragment time-of-flight wall TOFd and the fiber tracking detector Fi4. Raw data in MBS format was unpacked and hardware channels were mapped to physical detector indices using the UCESB (Unpack and Check Every Single Bit) software tool. The experiment resulted in a successful test of the reconstruction chain up to the HIT level for LOS, PSPx and TOFd detectors. The online histogram server was configured and used for monitoring in online mode. Fi4 still requires both hardware and software development. Previously, based on the data from s438b experiment in 2015, the fully automated calibration procedure for NeuLAND neutron detector was developed [4]. Work is ongoing towards completion of the list of detectors with calibrated and reconstructed HIT data in order to proceed to the high-level physics analysis.

Status of simulations

The level of the simulations for detectors like CALIFA (gamma spectrometer), NeuLAND (neutron detector) [5] and VETO wall is advanced (including granular and detailed geometry description) and the results have previously contributed to the Technical Design Reports of the first two. Improvement of the description of the geometry and calculation of the response for other detectors is in progress and is currently focused on the preparations for the upcoming beam-time in 2018 at SIS18. There are also ongoing activities on the selection and validation of a Geant4 physics list suitable for the R^3B physics as well as on the design of classes for data levels in order to merge simulation and data analysis on the framework level.

References

[1] R^3B: https://www.gsi.de/r3b
[2] R3BRoot: https://www.r3broot.gsi.de
[3] M. Al-Turany *et al.* J. of Phys. Conf. Ser **396** (2012) 022001
[4] V. Wagner *et al.*, this annual report
[5] J. Mayer *et al.*, this annual report

---

[*] d.kresan@gsi.de

DOI:10.15120/GR-2017-1

DDS: The Dynamic Deployment System

A. Manafov[1] *and A. Lebedev*[1]
[1]GSI, Darmstadt, Germany

The Dynamic Deployment System (DDS) [1] is a toolset that automates and significantly simplifies a deployment of user defined processes and their dependencies on any resource management system (RMS) using a given topology.

During 2016 DDS development has been focused on improvements of the core code and main modules.

Shared memory communication. In the initial implementation dds-agents used to have only a network connection transport for communication with user tasks. This introduced certain implications, for instance, there was no guarantee that all key-value updates or custom command messages will be delivered to the user. As a fallback solution a shared memory was used to cache messages comming from network channels, to make sure that all messages are actually delivered to the user tasks. In order to improve and simplify this algorithm we have implemented a generic shared memory channel. The channel has similar API as DDS network channel, it supports two way communication, asynchronous read and write operations. Its implementation is based on the boost::message_queue library [2], on the DDS protocol which is used for message encoding and decoding and on the boost::asio library [2] for thread poolling and implementation of the proactor design pattern. The shared memory channel is used for communication between dds-agents and user tasks which significantly simplifies and secures the implementation (see Figure 1). There is no need to cache messages any more as we now can guarantee the delivery. All messages are stored directly in the shared memory and managed by the message queue. The new implementation shows a factor of 2 better performance in our test case where 40 tasks intensively exchanging key-values on a single node with 40 logical cores. It is also forseen that the new shared memory channel will be used in other parts of DDS, for example, for communication between dds-agents on the local machine.

New dds-intercom library API. With the release of the shared memory channel we have also introduced a new version of the dds-intercom library API.

Versioning in key-value propagation. In DDS a single property in the topology results in multiple keys at runtime, namely, each task gets its own key for a certain property. A given task can only change a key it owns. But in some edge cases a versioning of key-value pairs is required to protect against key updates with an obsolete values. For instance, if task sends a key-value, crashes and then restarts and sends it again. In some cases the key update which was send first can be processed after the key update which was send last. As a result there will be a wrong value assigned to the key.

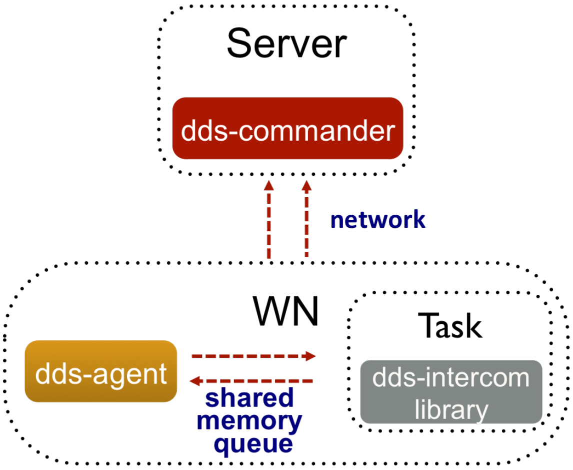

Figure 1: New shared memory communication.

The versioning prevents such situations. Its implementation is completely hidden from the user, all versioning algorithms are processed by DDS behind the scene.

Runtime topology update. In 2016 we have also introduced a runtime topology update feature to offer users a possibility to make changes in a currently running topology without stopping it. The algorithm determines the difference between old and new topologies on the fly. As a result it creates lists of tasks and collections that has to be added and removed. These lists are passed to DDS scheduler which then applies required changes by sending commands to corresponding DDS agents.

RMS plugins. Newly developed LSF and PBS plugins were added to the list of supported DDS RMS plugins.

Automated tests using dds-octopus. Growing complexity of DDS requires powerful functional tests, as most of issues can only be detected during runtime when multiple agents are in use. Unit tests can't cover all edge cases. We therefore introduced a dds-octopus tool chain - a full blown functional test machinery for DDS. dds-octopus features a rapid development of test cases with minimum code duplication. The tool chain is designed to run fully automatic without human intervention. Since DDS 1.4 it runs as a part of continues integration builds.

References

[1] The Dynamic Deployment System (DDS), http://dds.gsi.de.

[2] The BOOST C++ Libraries, http://boost.org

DOI:10.15120/GR-2017-1

FairDb status

D. Bertini[1]
[1]Scientific Computing, GSI, Darmstadt, Germany

FairDb is a virtual database library which extends the FairRoot[1] framework initialization scheme to any SQL compliant database systems. This report describes the present FairDb status.

Introduction

FairDB provides the user with a well-defined and uniform API for database manipulation. Using internally the ROOT `TSQLServer` class [2], the same user code can be executed independently on Oracle, MySQL, PostGreSQL and even SQLite SQL database engines (Fig. [1]).

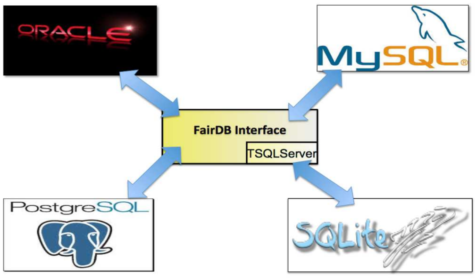

Figure 1: FairDB supported SQL-Database engines.

Generic parameter template

A new generic paremeter interface has been implemented in order to ease the writing of parameter container. The new interface uses the Curiously Recurring Template Pattern (CRTP[4]) to automatically generate all the neccessary functions to perform input and output operations. The user can then focus on the more important task of choosing and designing the parameter data model.

Caching

In order to reduce the response time FairDb stores the data in a client cache memory or cache file using a dedicated serialization procedure. When queries are executed repeatedly, the user application retrieves results directly from the client cache, resulting in faster query response time (Fig. [2]).

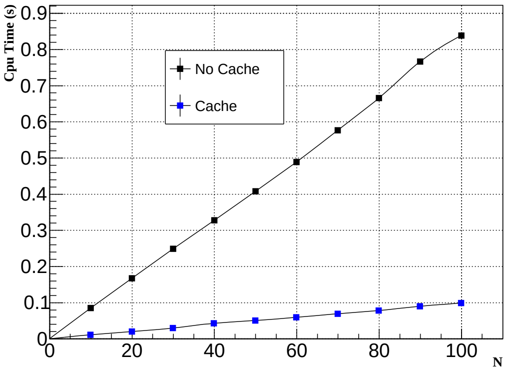

Figure 2: Query response time as a funtion of the number of parameter initialised with and without caching mechanism.

Sts Qa web interface

The Sts Qa web interface has been completely redesign to cope with automatically attributed sensor unique identifier. The query of sensor quality information is done via the vendor production batch number. Fig. [3] shows a snapshot of the new Sts Qa web interface.

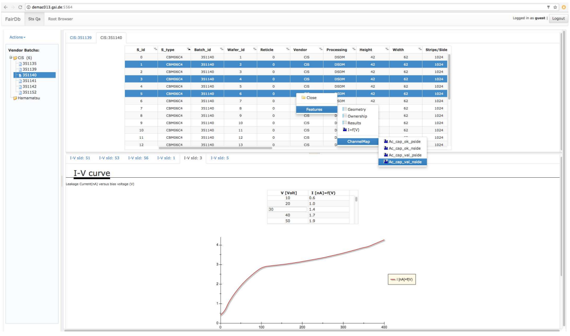

Figure 3: Sts Qa interface

References

[1] The FAIR simulation and analysis framework 2008 J. Phys.: Conf. Ser. 119 032011

[2] R. Brun, F. Rademakers, P. Canal, I.Antcheva , D. Buskulic, O. Couet, A. and M. Gheata *ROOT User Guide* CERN, Geneva 2005.

[3] FairRoot Virtual Database (User Manual) `https://cbm-wiki.gsi.de/foswiki/pub/STS/STSComponentsDatabase/FairDB_Manual.pdf`

[4] `https://en.wikipedia.org/wiki/Curiously_recurring_template_pattern`

DOI:10.15120/GR-2017-1

Lattice QCD Dslash operator implementation on FPGA accelerator with data-flow computing*

T. Janson, and U. Kebschull[1]
[1]IRI Goethe University, Frankfurt, Germany

Introduction

In this work we investigate new methodologies to compute Lattice QCD algorithms using data-flow computing. The algorithm is described and programmed as a graph that models the data movement through arithmetic compute nodes. This can be seen as the opposite of programming the control flow for traditional von Neumann computers, where one programs or models the flow of control commands. The concept data-flow programming is also discussed in [1, 2]. Such a graph is programmed with MaxJ from Maxeler and will run on DataFlow machines from the same company. For this, Maxeler provides a framework to develop, simulate, and run such applications. The goal is to figure out if we can accelerate Lattice QCD simulation with this framework.

Data-flow computing is not a new approach and goes back to works from Jack B. Dennis and many others since the beginning of 1970s [3]. We use the concept developed from Maxeler called Multiscale DataFlow Computing [4] that combines approaches like static and dynamic data-flow principles, and vector or array processing to scale the features of a compute problem on different levels of computation finding an optimal solution.

The Framework

The framework consists of a data-flow machine node (MPC-X) and a CPU host computer [5]. Both are interconnected with Infiniband. Figure 1 shows the architecture. Further, the software part is divided into a data-flow compiler, which compiles the MaxJ code into a configuration bit file for the MPC-X node, and a run time system that controls and schedules the configuration and execution of data-flow engines (DFE). Each MPC-X can host eight DFEs, where each has 96 GByte DDR3 memory over six channels connected, which is called large memory (LMem). In addition, all DFEs form a ring structure to stream data between data-flow engines. It is possible to connect several CPU host computers and MPC-X nodes over an Infiniband network to form a supercomputer. This study is done on one CPU host and one MPC-X with four DFEs.

Dslash Operator as Data-Flow Graph

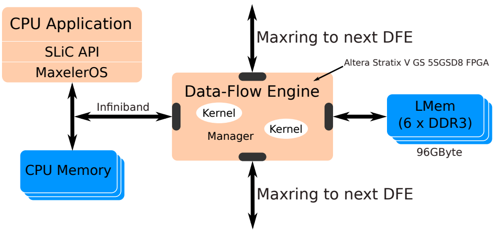

Figure 1: Maxeler System Architecture

We use the Wilson Dirac operator described in [7, p.115] that performs $\Psi'(n) = (1 - \kappa H)\,\Psi(n)$, where the hopping matrix H collects all nearest neighbour terms. Here, n is a four dimensional vector (x, y, z, t) and labels lattice sites. For each site index n we compose a data structure with one spinor and its four link variables to be held in LMem as an array of structure (AoS). Read or write commands to the LMem fetch these data structures in bursts of 384 Byte using a linear access pattern. The indexing scheme of the data-flow stream and also the storage order in LMem is given by $n = x + y * N_s + z * N_s^2 + t * N_s^3$ with spatial lattice extent parameter N_s.

The implemented data-flow kernel graph for one direc-

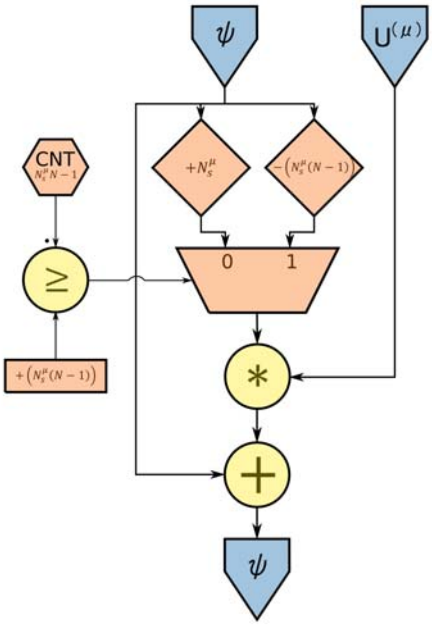

Figure 2: Data-flow graph for one lattice coordinate in forward direction which collects one neighbour term

---

* Work supported by HIC for FAIR and HGS-HIRe

DOI:10.15120/GR-2017-1

tion μ is shown in figure 2. Such a directed kernel graph contains a small set of node types and arcs [5]. Data flows along the arcs and through the fully pipelined nodes. Circles in a graph are arithmetic and logic operations, rectangles provide constant parameters, and diamonds implement the offset operator. In addition, there are multiplexer nodes, counter cores, and last I/O nodes. A program describes the graph with MaxJ/Java syntactic code [5, 6]. As in Java, one can define methods for complex operations like matrix vector multiplications which are then sub graphs in a kernel. This way, we have implemented the Dslash as shown partly in figure 2 to collect all neighbours simultaneously. Here, the offset operator picks up the nearest neighbour terms within the data-flow stream. All arithmetic operations down to simple additions and multiplications are pipelined. Each core is running fully parallel on hardware. The offset parameters are derived from lattice extents and known at compile time. These parameters express data locality and the offset core allocates BRAM on an FPGA for larger offsets. It is the MaxJ compiler which creates VHDL code from the graph and distributes the local memory resources in a optimal way near to the compute cores.

Implementation Results and Outlook

We have implemented the Wilson Dirac operator in single precision, which fits completely on an Altera Stratix V FPGA (MAX4) using fixed-point arithmetic. The resource usage is shown in table 1. It should be noted that the algorithm is implemented as a full data-flow graph that collects all nearest neighbour terms to perform all vector and matrix multiplications as well as additions in one kernel tick. This allows us to update one spinor collecting all neighbour terms in one clock cycle. The so implemented operator is memory bound with an equivalent arithmetic intensity of 0.92 FLOPs/Byte. With 133 MHz kernel clock frequency, we get a equivalent theoretical peak performance of 176 GFLOPs. We use the term ”equivalent” here, because our implementation is using fixed-point arithmetic. Each site is read or written only once from or to the LMem using a linear access pattern to get the best possible memory bandwidth. To collect all neighbours, it is necessary that the lattice fits completely into BRAM, which restricts our size to $16^3 \times 4$. Thus, we have developed a custom memory command generator to access the LMem also for any bigger lattice divided into tiles, where one tile will be computed with the Dslash implementation described above. The communication with neighbour tiles is performed over halo buffers. The focus is to improve the memory access to get the highest possible performance. Each tile as well as the lattice itself is a four dimensional hypercube. The surrounding next neighbour tiles, the surface for such a cube, are three dimensional volumes. There are eight neighbours. The idea is to stream the tiles through a DFE in one direction that way to get the best possible linear memory access on the LMem, where we need six halo buffers to the other directions. Tests have shown that we can reach a peak performance of 25 GByte/s using a custom memory command generator which is only the half LMem peak performance of 48 GByte/s. Therefore, we have to improve the LMem interface, which is still an ongoing process. In addition, a first test against a given data set show a relative error of $10^{-4}\%$ compared to exact values computed with Mathematica.

Resource Usage				
Logic utilization	114771	/	262400	(43.74%)
Primary FFs	203944	/	524800	(38.86%)
Secondary FFs	5810	/	524800	(1.11%)
Multipliers	2304	/	3926	(58.69%)
DSP blocks	1152	/	1963	(58.69%)
Block Memory	2489	/	2567	(96.96%)

Table 1: Resource usage of implemented Dslash operator processing $\Psi'(n) = (1 - \kappa H)\,\Psi(n)$ to collect all neighbour terms

References

[1] F. Gruell and U. Kebschull, “Accelerating of Biomedical Image Processing with Dataflow on FPGAs“, River Publishers, 2016, ISBN 978-87-93379-36-7

[2] V. Milutinović, J. Salom, N. Trifunovic, R. Giorgi, “Guide to DataFlow Supercomputing“, Springer, 2015, ISBN 978-3-319-16229-4

[3] J. B. Dennis and D. P. Misunas, “A preliminary architecture for a basic data-flow processor“, ISCA’75, ACM, 1974, p. 126–132

[4] O. Pell (Maxeler), “Keynote: Multiscale Dataflow Computing“, 6th International Workshop on Multi-/Many-core Computing Systems (MuCoCoS-2013), Edinburgh, UK, 2013

[5] Maxeler Technologies, “Programming MPC Systems“, White Paper, June 2013

[6] OpenSPL Consortium, “OpenSPL: Revealing the Power of Spatial Computing“, White Paper, Dec 2013

[7] C. Gattringer and C. B. Lang, ”Lecture Notes in Physics 788: Quantum Chromodynamics on the Lattice”, Springer, 2010, ISBN 978-3-642-01849-7

DOI:10.15120/GR-2017-1

Testing of new sensitive TLD cards

E.Kozlova[1]*, A. Sokolov* [1]*, M. Pyshkina* [2]*, and T. Radon*[1]
[1]GSI, Darmstadt, Germany; [2]Ural Federal University, Yekaterinburg, Russia

Introduction

During the GSI accelerator facility operation the radiation fields outside the shielding are dominated by the neutron component which is monitored among others with a passive thermoluminescent based dosimeter. The sensitive elements are thermoluminescent crystals. They are situated in the center of a polyethylene moderator. In order to improve the response to high energy neutrons the moderator is equipped with a lead layer. Each sphere is equipped with one card carrying pairs of TL 600/700 crystals [1].

In some cases it is required to measure small doses which can hardly be distinguished from the natural background. In this work, the sensitivity threshold for new TLD cards and previously used TLD cards was determined.

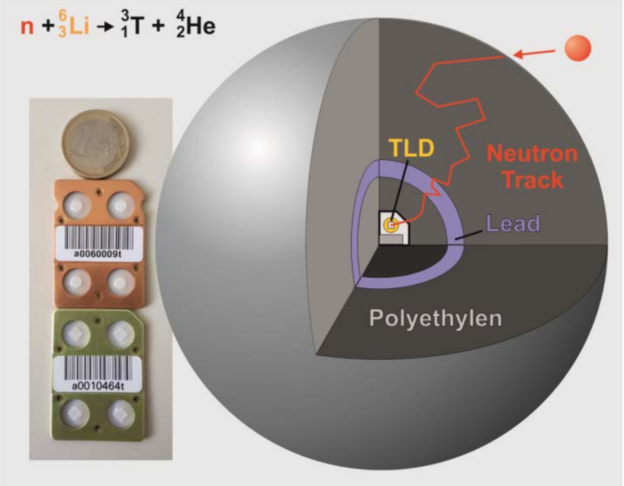

Figure 1: Schematic view of the GSI sphere with a TLD card. The radius of the sphere equipped with lead is 16,25 cm. Previously used TLD (yellow) and new (orange) TLD cards are shown in comparison with a one Euro coin.

Measurements

Spheres containing two type of TLD cards were positioned in one meter distance from a 37 GBq (1 Ci) ^{241}Am(α,n)Be neutron source. An ambient dose equivalent of 21,1 µSv per hour was delivered by the source at the position of the spheres. The cards inside the spheres were irradiated for 15 minutes, 30 minutes, 1 hour, 2 hours and 4 hours. The new TLD cards were additionally irradiated for 7 minutes.

Results

The results of the experiment are presented in Fig 2. Relative deviations of the measured ambient dose equivalent from the expected are calculated for old and new TLD cards. The deviations are plotted versus the expected doses. It can be clearly seen that the old TLD cards might be used for doses above 20 µSv only and the new TLD cards might be used for smaller dose measurement down to ~2 µSv. Thus new TLD cards are more suitable for the area monitoring with low dose rates. Similar results are produced by the spheres without lead layer.

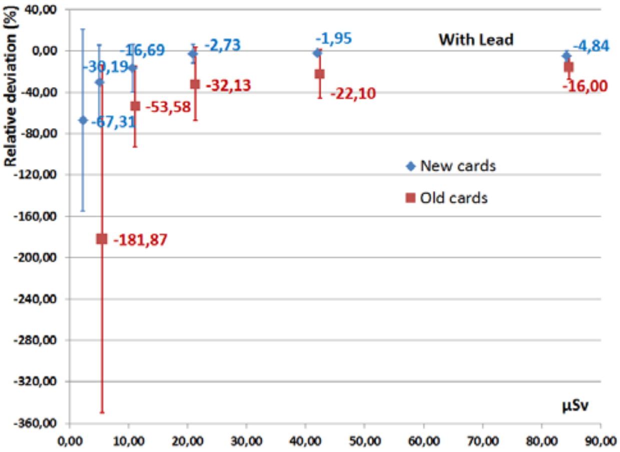

Figure 2: Relative deviation of measured ambient dose equivalent values from calculated values.

The calibration of the detectors was performed by also using a ^{241}Am(α,n)Be neutron source. The energy dose response of the bare thermoluminescent elements was determined with a ^{137}Cs γ-source before the cards can serve as neutron detectors. The corresponding values are stored for every card in the automatic TLD reader [2]. The calibration factors for the spheres with lead and without lead with two types of the TLD cards are listed in Table 1. The calibration factor is defined as the ratio of the measured energy dose response in Gy and the expected dose equivalent from the source in Sv.

Table 1. Calibration factors for the TLD cards situated in the spheres with and without lead layer.

Detector	New	Old	unit
With Lead	0,83±0,05	2,40±0,03	Gy/Sv
Without Lead	0,88±0,05	2,82±0,09	Gy/Sv

References

[1] F. Gutermuth et al., The response of various neutron dosemeters considering the application at a high energy particle accelerator, Kerntechnik, 68, 172-179 (2003)

[2] Thermo Scientific Harshaw 6600 PLUS TLD Reader, https://tools.thermofisher.com/content/sfs/brochures/Harshaw-6600-Brochure.pdf

DOI:10.15120/GR-2017-1

Neutron dosimeters for the high energy accelerators

A. Sokolov[1]*, G. Fehrenbacher*[1,2]*, E. Kozlova*[1]*, T. Radon*[1]
[1]GSI, Darmstadt, Germany; [2]now at Uni. Tübingen, Germany

High energy accelerator facilities are sources of harmful radiation which should be continuously surveyed during operation. Neutrons in a wide energy range are one of the main contribution factors to the radiation, thus a reliable neutron dosimeter for radiation control is required. The present passive neutron dosimeter "GSI Ball" [1] is sufficient for the measurement of doses caused by neutrons from thermal up to 100 GeV energies; still it has a rather large size and weight.

Recently we have used the Monte Carlo code FLUKA [2] to study different layouts of passive neutron dosimeters. The passive dosimeter signal is proportional to the absorbed energy in the sensitive element, in our case it is a thermoluminescence detector (TLD) card. The response function in terms of absorbed energy of the TL chips irradiated in neutron fields has been calculated. The simulations revealed a possibility to create a compact neutron dosimeter [3]. The chosen design was manufactured and tested at the CERF [4] facility at CERN. The results approved the simulation approach and confirmed the possibility to use the dosimeter in high energy neutron fields [5].

Our further design developments improving the dosimeter response brought us to the dosimeter depicted in fig.1 (left).

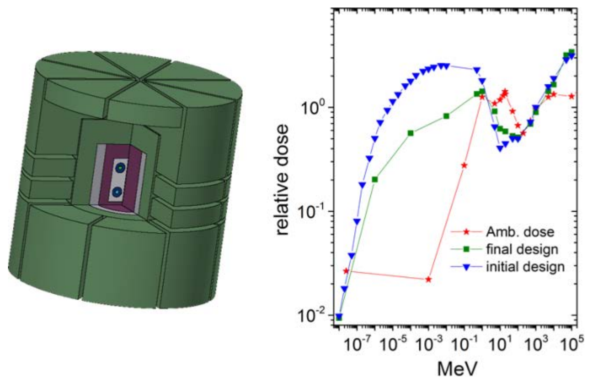

Figure 1. Left: Neutron dosimeter in 3D view (obtained using Flair [6]) with openings in the outer PVC layer (green). The inner lead (grey) and PE (purple) layer with a TLD card in the middle can be seen. Right: The final dosimeter response in comparison to the required ambient dose values and additionally the response function for the dosimeter from [3] are shown.

The initial design [3] was slightly increased to 20 cm in height and 20 cm in diameter. Openings were cut into the highly absorptive PVC layer to make the dosimeter more transparent to thermal neutrons. The final response is improved in comparison to the previous design fig.1 (right) and can even be further improved increasing the size of the dosimeter.

FLUKA is capable to calculate isotope production rates under neutron irradiation. Several simulations were performed to count the number of ^{3}H and α-particles produced in TLD chips during the detection time. In the TL chips the Li^6 element is used to detect neutrons via the ^{6}Li(n,α)^{3}H reaction. The calculated amount of tritium and alphas revealed the same dosimeter response function as the first method, which takes into account the absorbed energy.

The method calculating the amount of e.g. ^{3}H – particles is very suitable to estimate the dose reading of the active detectors, where the dose is calculated as a number of pulses. Each pulse corresponds to a neutron capture event. In a couple of tests we have also performed some simulations calculating the tritium production for the active ^{3}He dosimeters. The neutrons are detected here via the ^{3}He(n,p)^{3}H reaction. Again we additionally used the absorption energy for detection and both methods gave the same response, within a statistical uncertainty of around 5 %.

After the response calculations of the passive dosimeters with a TLD card, as the sensitive element, we wanted to check the studied layouts to be used for the active neutron dosimeters with a ^{3}He counter tube as the sensitive element. The energy dependency of the capture cross sections for ^{3}He and ^{6}Li are pretty similar, thus it is interesting to check the response of a possible neutron dosimeter with a ^{3}He proportional counter instead of the TL chips.

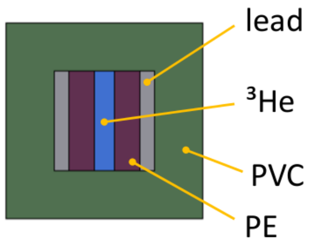

Figure 2. Compact dosimeter with a PVC layer and a ³He tube in the centre.

The readings of the dosimeters shown in Fig. 2 containing a cylindrical volume, 1.4 cm in diameter, filled with ^{3}He gas at 1 bar pressure shows identical readings as the one with a TLD card from [3]. The readings for the active dosimeters were obtained counting the neutron capture reactions as was described above, still in simulations the steel tube containing the ^{3}He gas and connections were not included and in reality can slightly influence the response characteristics, as well as the different gas pressures of the counter. Exchanging the sensitive element of the dosimeter in all layouts studied in [7], including the one from fig.1, should provide almost the same read-out

DOI:10.15120/GR-2017-1

values. The active dosimeter prototypes are to be tested in the near future.

The new design from fig.1, though it is larger than the initially proposed one [3], is still only half as heavy as the currently used dosimeter. In comparison to the initial design, which showed around 20 % higher dose values at the CERF experiment [5], the new design should provide exact values.

References

[1] G. Fehrenbacher, F. Gutermuth, E. Kozlova, T. Radon and R. Schuetz, Neutron dose measurements with the GSI ball at high-energy accelerators, Radiation Protection Dosimetry (2007), Advance Access publication 16 September 2007, Vol. **125**, No. 1-4, pp. 209-212.

[2] A. Fasso‘, A. Ferrari, J. Ranft and P. R Sala, FLUKA: a multi-particle transport code, CERN-2005-10 (2005), INFN/TC 05/11, SLAC-R-773.

[3] A.Sokolov, G. Fehrenbacher, E.Kozlova, T.Radon, “ANDREA, a Compact Neutron Dosimeter”, GSI Scientific report 2014

[4] A. Mitaroff and M. Silari, The CERN-EU high-energy Reference Field (CERF) facility for dosimetry at commercial flight altitudes and in space, Radiation Protection Dosimetry 102, 7-22, 2002.

[5] I.A. Zahradnik, Development of the passive neutron dosimeter, ANDREA, for high energy accelerators, verification measurements and simulation of the dose response using the Monte Carlo code , bachelor thesis, THM Giessen (2015).

[6] V. Vlachoudis, FLAIR: A Powerful But User Friendly Graphical Interface For FLUKA Proc. Int. Conf. on Mathematics, Computational Methods & Reactor Physics (M&C 2009),, Saratoga Springs, New York, 2009.

[7] “Design Development of a passive neutron dosimeter for the use at high energy accelerators”, A. Sokolov, G.Fehrenbacher, T. Radon, Radiation Protection Dosimetry 2015;doi: 10.1093/rpd/ncv489

DOI:10.15120/GR-2017-1